J. Appl. Comput. Mech., xx(x) (2026) 1-18
DOI: 10.22055/jacm.2026.49665.6145

ISSN: 2383-4536
jacm.scu.ac.ir

Shahid Chamran University of Ahvaz

Journal of Applied and Computational Mechanics



Research Paper

From Elements to Energy: A Controlled Benchmark of Finite Element, Element-Free Galerkin, and Deep Energy Methods in Solid Mechanics

Tianhui Yang[1], Ammar Qarariyah[2]

[1] School of Science, Xi'an University of Posts and Telecommunications, Xi'an, Shaanxi 710121, PR China, Email: yth.tianhui@xupt.edu.cn

[2] Department of Technology, Bethlehem University, 5 Rue des Frères, Bethlehem P1520468, Palestine, Email: aqarariyah@bethlehem.edu

Received August 02 2026; Revised October 04 2026; Accepted for publication October 12 2026.
✉ Corresponding author: A. Qarariyah (aqarariyah@bethlehem.edu)
© 2026 Published by Shahid Chamran University of Ahvaz

Abstract. Computational solid mechanics is dominated by mesh-based discretizations, while meshless and physics-informed approaches have emerged as alternatives. This study benchmarks three specified displacement formulations for two-dimensional linear elastostatics: full-integration bilinear quadrilateral finite elements (Q4 FEM), first-order moving-least-squares Element-Free Galerkin (EFG), and a four-hidden-layer tanh Deep Energy Method (DEM). The contribution is a controlled cross-paradigm assessment under one multi-regime protocol. On smooth problems, the three tested implementations achieve comparable accuracy. For the near-incompressible plane-strain cantilever, the tested Q4 FEM implementation underestimates tip displacement by 80.36%, whereas the tested EFG configuration reaches 0.33% error. Six of twenty baseline DEM runs return non-finite values, and the lowest-loss finite run has a 77.54% tip-displacement error. A matched-parameter depth study further confirms optimizer-stage sensitivity. Shared post-processing changes the interpretation of the localized results: FEM and EFG are close on the common near-hole ring, while the converged common-grid crack check preserves the FEM-EFG-DEM ordering for the specified implementations. Across the sampled trials, final DEM loss is informative for some bulk measures but weakly or inversely associated with localized or selected engineering errors. Reporting only the minimum-loss trial can therefore conceal non-finite outcomes and the observed error distribution; seeded errors and failure frequencies should accompany loss-based model selection.

Keywords: Finite element method; Element-Free Galerkin method; Deep Energy Method; linear elasticity; physics-informed learning.

1. Introduction

The finite element method (FEM) has been the dominant computational framework for linear elastostatics for several decades owing to its rigorous mathematical foundation, mature verification procedures, efficient sparse linear algebra, and widespread industrial adoption. Its success has established FEM as the reference methodology for most computational solid mechanics applications. Alongside FEM, two alternative approximation paradigms have developed. Meshless methods eliminate element connectivity by constructing approximation spaces directly from scattered nodes, while physics-informed machine learning replaces conventional discrete basis functions with trainable neural networks that satisfy the governing equations through optimization. Among these alternatives, the Element-Free Galerkin (EFG) method [1] has become one of the most extensively studied meshless formulations, whereas the Deep Energy Method (DEM) [2] has emerged as a representative energy-based neural approach for elasticity. Although all three formulations seek the same continuum solution, they differ fundamentally in their approximation spaces, numerical integration procedures, enforcement of essential boundary conditions, and computational workflows.

Extensive studies exist within each methodological family. Low-order finite elements are susceptible to shear and volumetric locking in nearly incompressible materials. Meshless methods have been reviewed with respect to approximation accuracy, support-domain construction, numerical integration, computational efficiency, and the treatment of essential boundary conditions for non-interpolatory moving-least-squares approximations [3-5]. Li and Li [6] recently proposed gradient polynomial smoothing integration with explicit quadrature and arbitrary-order basis functions for Galerkin meshfree methods. Physics-informed learning has also been reviewed as a mesh-independent framework for partial differential equations [7]. These reviews identify optimization sensitivity, computational cost, hyperparameter dependence, reduced accuracy near discontinuities or singular fields, and nonstandard validation practices as continuing limitations. Many reported studies use relatively simple benchmarks, and direct comparisons with established numerical methods remain limited.

Published online: November 7 2026

Direct comparisons between neural energy methods and classical discretizations have begun to emerge. Thombre et al. [8] compared several energy-based neural formulations with FEM for two-dimensional elasticity and proposed modifications for traction-free boundaries and stress concentrations. Grossmann et al. [9] compared PINNs with FEM in solution accuracy and computational time and emphasized the importance of reproducible, accuracy-based comparisons. Other studies have examined modified loss functions, three-dimensional extensions, and optimization strategies for physics-informed elasticity [10,11]. These studies primarily compare neural variants with finite elements, whereas meshless reviews compare formulations within the meshless family. Comparisons that include finite-element, meshless, and physics-informed formulations within one benchmark remain limited.

Comparisons between broad method families require careful control of implementation choices. Performance depends on approximation order, numerical integration, boundary-condition enforcement, support size, neural architecture, activation function, optimization algorithm, and refinement strategy. Results from one implementation therefore do not define family-wide behavior. A controlled comparison must specify the baseline formulations, apply a common physical protocol, and retain the formulation-specific features that cannot be made identical.

The objective of the present work is to provide such a controlled benchmark. Rather than proposing a new numerical method, this study performs a systematic comparison of three specified displacement formulations for two-dimensional linear elastostatics: full-integration Q4 FEM, first-order MLS EFG with penalty enforcement of essential boundary conditions, and fully connected tanh DEM trained by Adam followed by L-BFGS. To the best of our knowledge, no previous study has evaluated representatives of these three paradigms simultaneously on a multi-regime elastostatic suite while combining common physical definitions, common-point checks for localized quantities, an independent high-order Cook reference, trial-level loss-error auditing, and accuracy-matched timing comparisons.

The benchmark comprises five problems that collectively span several representative accuracy regimes encountered in computational solid mechanics, including constant-strain consistency, bending-dominated deformation, near-incompressibility, smooth curved stress concentrations, and crack-tip singularities. All formulations solve the same continuum boundary-value problems with identical geometry, loading, and material parameters, and are assessed using common definitions of displacement, strain energy, and problem-specific error measures. At the same time, formulation-specific ingredients—including numerical quadrature, constraint enforcement, discretization variables, and optimization procedures—are intentionally retained because they constitute intrinsic characteristics of the respective methods rather than experimental inconsistencies. The objective is therefore not to force identical discrete systems, but to compare representative implementations under equivalent physical conditions and common evaluation criteria.

The unified protocol reveals accuracy patterns that are not visible from isolated single-method studies. The three tested implementations achieve comparable accuracy for sufficiently smooth problems. For the near-incompressible cantilever, Q4 FEM exhibits volumetric locking, the tested EFG configuration remains largely locking-free, and the tested DEM configuration produces six non-finite runs together with an inverse loss-error ordering despite increased training effort. For the localized hole and crack quantities, the tested FEM implementation has lower errors than the tested EFG and DEM implementations. The method-specific values are not resolution-matched, but common-point post-processing at the hole and crack preserves this ordering for the selected local metrics. The comparison also shows that localized quantities distinguish the computed fields more strongly than global energy measures. DEM training loss is informative for some bulk quantities but is weakly or inversely associated with localized accuracy in the sampled near-incompressible cantilever runs.

This study makes four contributions. First, it establishes a controlled cross-paradigm benchmark across five elastostatic regimes and limits its conclusions to the selected formulations. Second, it combines common definitions of the reported quantities with shared-point post-processing for the hole and crack and an independent Q8 convergence reference for Cook's membrane. Third, it reports trial-level DEM loss and error and evaluates depth and optimizer-stage sensitivity at nearly fixed parameter count. These results show that the minimum-loss run alone does not characterize non-finite outcomes or the error in a selected quantity of interest. Fourth, it compares computational effort through error-versus-wall-clock results and common accuracy thresholds without treating neural parameters as equivalent to nodal displacement unknowns.

This work does not seek a universal ranking of FEM, EFG, and DEM. Low-order element locking, MLS non-interpolation, and neural optimization sensitivity are established results. The comparative results show how these effects depend on the problem regime and quantity of interest under one protocol: the selected localized ordering persists under common-point post-processing, DEM loss-error ordering changes across quantities, network depth affects accuracy and non-finite-run frequency at nearly fixed capacity, and comparable accuracy is reached at different measured costs.

The remainder of the paper is organized as follows. Section 2 positions the three formulations within their broader methodological families. Section 3 presents the benchmark design and evaluation protocol. Section 4 describes the common continuum formulation and the formulation-specific discretizations. Section 5 reports the numerical results and analyzes accuracy, robustness, and computational performance. Sections 6 and 7 discuss the implications and limitations, and Section 8 summarizes the conclusions.

2. Taxonomy of Discretization Paradigms

Figure 1 and Table 1 summarize the taxonomy of discretization strategies relevant to this comparison.

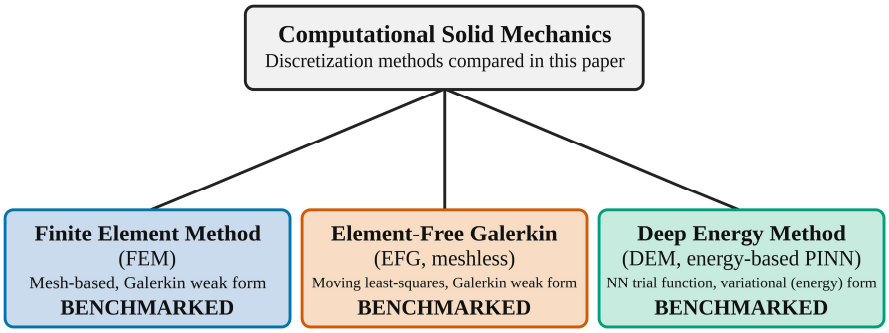


Fig. 1. Taxonomy of approximation spaces and solution strategies for two-dimensional linear elastostatics, organized into mesh-based (FEM), meshless (EFG and related methods), and physics-informed learning (DEM and related methods) families, as considered in this benchmark comparison.

Table 1. The three baseline formulations tested in this paper. The EFG row specifies the basis order used in this study; EFG also permits higher-order MLS bases. The last column lists implementation features that must be considered when interpreting the results; it is not a ranking of method families.

Tested formulation	Trial representation and solve	Interpretive feature in this study
Q4 FEM	Bilinear, interpolatory Galerkin basis on a conforming mesh; sparse direct linear solve	Full integration is susceptible to locking near incompressibility; local crack accuracy depends on mesh grading and the interaction-integral extraction
Penalty EFG	First-order MLS Galerkin basis on scattered nodes (configuration used here); arbitrary-order MLS bases are also possible	Non-interpolatory essential-boundary treatment and support/integration choices affect conditioning and local stress accuracy
Tanh DEM	Four-hidden-layer fully connected network; energy minimization by Adam and L-BFGS	Stochastic non-convex optimization, architecture dependence, and weak coupling between bulk energy and localized quantities of interest

2.1. Three benchmark paradigms

FEM, EFG, and DEM represent three distinct trial representations of the same underlying energy functional: piecewise-polynomial basis functions defined on a mesh, moving-least-squares approximations defined on scattered nodes, and a nonlinear neural-network parameterization optimized through energy minimization. Each has been reviewed extensively within its own family. Classical FEM behavior, including its well-documented shear and volumetric locking at near-incompressible Poisson ratio, is textbook material. Meshless methods have their own comparative reviews [3-5], and physics-informed neural networks for solid mechanics have likewise been surveyed [7]. None of these reviews positions the three paradigms against one another on a shared benchmark suite, a gap Section 2.6 returns to after the three families are introduced below.

The remaining subsections situate FEM, EFG, and DEM within their broader method families to identify the trial representation used by each formulation and its documented limitations. Figure 2 places these families within the wider discretization landscape, including the hybrid meshless-learning branch discussed in Section 2.5.

The taxonomy is used to separate formulation choices from method-family claims. The numerical results below apply to the three implementations in Table 1; enriched, mixed, stabilized, or adaptive variants can behave differently. The following subsections therefore identify the implementation features needed to interpret the benchmark rather than assigning a single inherent failure mode to each family.

2.2. Finite elements and enrichment extensions

The susceptibility of classical low-order FEM to shear and volumetric locking near incompressibility, together with limited accuracy for unresolved stress singularities, motivated enrichment strategies relevant to the crack and hole benchmarks. The extended finite element method (XFEM) [12-14], based on the partition-of-unity concept [15], enriches the standard FEM approximation with discontinuous and near-tip asymptotic functions so that a crack or hole boundary can be represented independently of the mesh. This differs from the conforming graded FEM mesh and domain-form interaction integral used here for K_I extraction. XFEM and related enrichment strategies specifically address singular fields, so their performance cannot be inferred from the unenriched FEM formulation examined in this study. The variational phase-field approach to fracture [16-18] represents Griffith's energy criterion [19] through a regularized damage field and an additional unknown. A comparative review [20] evaluates XFEM, mixed FEM, and phase-field models for quasi-brittle fracture, but it does not include the meshless and learning-based formulations considered here.

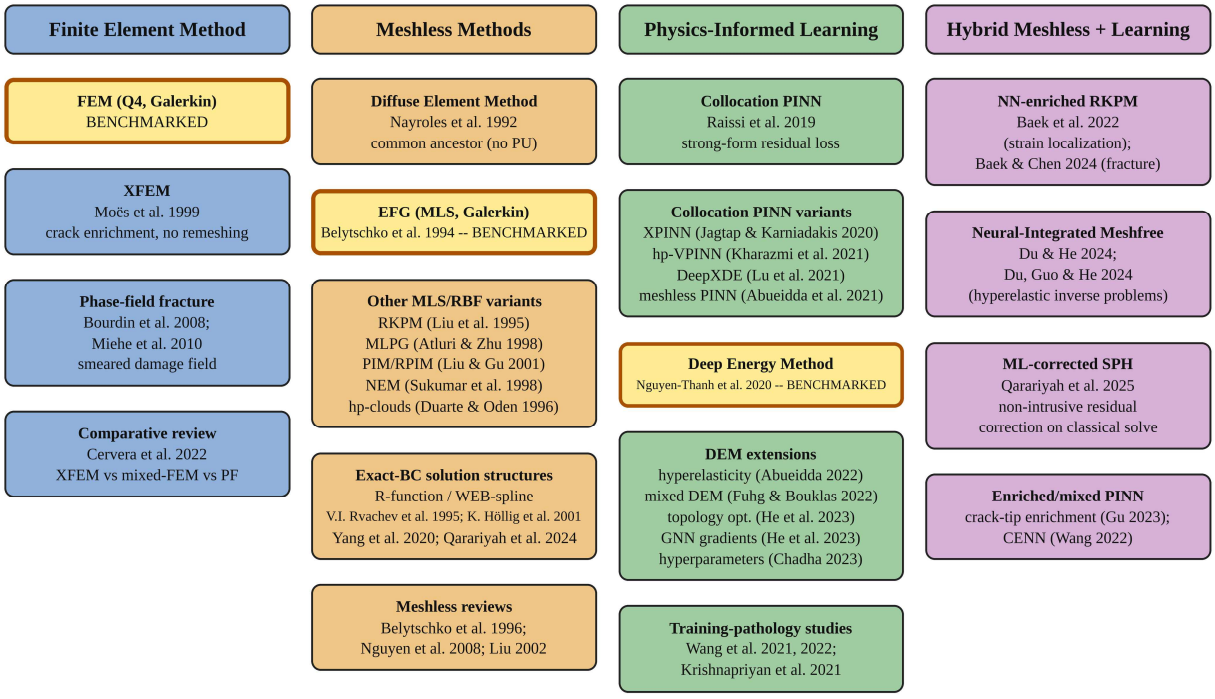


Fig. 2. The broader discretization landscape reviewed in this section, positioned against the three methods actually benchmarked in this paper (bold outlines). The hybrid meshless-plus-learning branch (right) has emerged only in the last two to three years.

2.3. The meshless family

EFG [1], this paper's benchmarked meshless representative, traces to Nayroles et al.'s earlier diffuse approximation method [21], and approximates the trial field using moving-least-squares (MLS) shape functions defined over a scattered node cloud rather than a mesh. This approximation is non-interpolatory, meaning nodal values are not the field values they label, which prevents boundary conditions from being enforced directly and motivates the penalty formulation used in this paper Eq. (17). EFG was selected as the meshless Galerkin baseline because it remains widely studied in solid mechanics and shares the same interior variational structure as FEM. Its near-incompressible behavior is not universal: locking depends on the support, integration, and formulation choices, as shown by both locking-free conditions and locking analyses in the EFG literature [22, 23]. The results below therefore describe the tested first-order MLS configuration, not EFG as a class. The same underlying MLS idea appears elsewhere in the wider meshless family, including the reproducing kernel particle method (RKPM) [24], the meshless local Petrov-Galerkin method [25], the h-p cloud method [26], and the point interpolation method [27], which recovers the interpolatory property EFG's MLS basis lacks at the cost of potential basis-matrix singularity. A related but geometrically distinct construction, the natural element method [28], instead builds interpolants from the Voronoi tessellation of the node set rather than an MLS moment-matrix fit, recovering exact nodal interpolation without that conditioning cost. Comprehensive treatments of this family, including the implementation details this paper's Section 4 draws on, are available elsewhere [3, 4]. What none of these treatments do, and what this paper's Sections 5 and Section 6 attempt, is hold a meshless representative to the same benchmark suite as FEM and a learning-based method simultaneously.

EFG's non-interpolatory shape functions and the resulting boundary-condition difficulty are not unique to this family. A separate meshfree-adjacent tradition, R-functions and the weighted extended B-spline method, enforces essential boundary conditions exactly rather than by penalty, by constructing a trial function that vanishes on the boundary by construction [29-32]. This is conceptually the same idea as this paper's DEM hard-constraint ansatz (Eq. (19), $u_\theta = u_D + d(\boldsymbol{x})\hat{u}_\theta$), independently arrived at in the meshfree and isogeometric-analysis literature, and it is directly relevant to this paper's natural (traction-free) inner boundary at the plate-with-hole's curved edge, the single hardest boundary condition for every method benchmarked here.

2.4. Physics-informed learning

Physics-informed neural networks (PINNs) [33, 34] minimize a strong-form PDE-residual loss using automatic differentiation in place of a mesh. The Deep Energy Method used in this paper instead minimizes the weak or energy form [35], following the variational computational-mechanics framework of Samaniego et al. [36] and related DEM developments [2]. The energy form was selected because it is the closest variational analogue to the weak formulations underlying FEM and EFG and requires only strain-level derivatives. These neural formulations must be distinguished from low-order finite-element locking. Lin et al. [37] showed that a mesh-free strong-form PINN can avoid the shear and volumetric locking observed in conventional low-order elements. Neural solvers therefore do not automatically inherit discretization-rooted element locking; the non-finite runs and adverse loss-error ordering observed here for the tested energy-based DEM are described as optimization instability, not as evidence of neural locking.

Subsequent PINN developments include domain-decomposed variants such as XPINN, cPINN, and FBPINN [38-40], as well as variational and hp-refined formulations that project residuals onto local polynomial test spaces [41]. Training analyses have identified gradient imbalance between residual and boundary terms [42], slow convergence for stiff problems [43], and non-convergence for some convection- or reaction-dominated problems [44]. Adaptive loss weighting has been proposed to address part of this sensitivity [45, 46]. This literature provides context for the optimization behavior reported here, where non-dimensionalization, an Adam-L-BFGS schedule, and multiple seeded trials are required. Software libraries such as DeepXDE [47] provide implementations of several collocation-based variants.

DEM has been extended to finite-deformation hyperelasticity [48], mixed displacement-stress approximation for concentration features [49], systematic hyperparameter and architecture studies [50], graph-neural-network gradient computation [51], and self-supervised topology optimization [52]. The architecture dependence reported in [50] is consistent with the sensitivity quantified in the present study. For singular fields, collocation PINNs enriched with Williams crack-tip functions improve crack-tip accuracy relative to an unenriched network [53]. These results support interpreting the crack-tip error reported here as a property of the tested unenriched energy-minimization configuration rather than a limit of energy-based learning as a method family.

2.5. Hybrid meshless-learning methods

Recent studies also combine meshless discretizations with learning components. Examples include neural enrichment of classical meshless kernels [54, 55], neural residual correction applied to a meshless solution [56], trainable networks embedded in meshfree partition-of-unity approximations [57,58], and trial functions constructed from radial basis functions with a particular-solution network [59]. These approaches retain different parts of the classical solver and therefore have approximation and optimization properties distinct from the three baseline formulations studied here. Hybrid methods are outside the present benchmark scope.

2.6. Research gap and contribution

Existing literature establishes Q4 locking, MLS boundary-treatment sensitivity, and neural optimization sensitivity. These behaviors have been documented separately, but their interaction has not been examined across a shared set of smooth, constrained, curved-boundary, and singular problems using common definitions of bulk and localized quantities. The remaining gap is a controlled experiment that separates deterministic spatial refinement from stochastic training while retaining formulation-specific numerical integration and constraint treatment.

The present study addresses this gap through matched physical boundary-value problems and common definitions of the reported quantities. Its contribution is implementation-level evidence obtained under one protocol: a Q4-EFG reversal between the near-incompressible cantilever and localized fracture measures; quantity-dependent association between DEM loss and engineering error; and measurable depth and optimizer-stage sensitivity at nearly fixed neural parameter count. The study does not assume identical discrete functionals, equivalent model sizes, or family-wide rankings.

3. Benchmark Scope and Reporting Protocol

The study uses five two-dimensional, small-strain, isotropic, static elasticity problems. The same geometry, material parameters, loads, and physical boundary conditions are used for the three formulations within each problem. Table 2 summarizes the benchmark purposes and references. A closed-form or standard analytical reference is used where available. For Cook's membrane, a separate Q8 convergence sequence supplies a high-order numerical reference independent of the benchmarked Q4 sequence; it is a converged numerical reference rather than an exact analytical solution.

Table 2. Physical benchmark suite. The crack comparison uses the nominal infinite-plate Irwin value; because the modeled domain is finite, this quantity is a reference metric rather than an exact solution of the finite square.

Problem	Geometry and material	Reference quantity	Primary purpose
Patch test	Distorted unit square; $E = 1000$, $\nu = 0.3$	Prescribed linear displacement field	Constant-strain consistency and boundary enforcement
Cantilever	$L = 48$, $D = 1$; $E = 3 \times 10^7$; $\nu = 0.3, 0.4999$	Timoshenko–Goodier displacement [60]	Bending response and sensitivity to near-incompressibility
Cook's membrane	Tapered panel; $E = 3000$; $\nu = 0.3, 0.4999$	Independent Q8 convergence reference	Distorted geometry and shear-dominated response
Plate with circular hole	Quarter domain; hole radius $a = 1$; $E = 1000$, $\nu = 0.3$	Kirsch field [61]	Smooth curved boundary and localized stress concentration
Center crack	Finite square; crack half-length $a = 1$; $E = 10^7$, $\nu = 0.3$	Nominal $K_I^\infty = \sigma\sqrt{\pi\, a}$ [62]	Singular-field resolution and stress-intensity extraction

The Cook domain has vertices $(0,0)$, $(48,44)$, $(48,60)$, and $(0,44)$, unit thickness, $E = 3000$, and plane-stress material response. The left edge is clamped and a uniform vertical traction $q_y = 1/16$ acts on the right edge, giving unit resultant force. The reported quantity is u_y at $(48,60)$. Figure 7(a) displays this model, and Figure 7(b) documents convergence of the independent Q8 reference.

The cantilever is analyzed in plane strain, with $L = 48$, $D = 1$, $E = 3 \times 10^7$, $P = 1000$, and $\nu = 0.3$ or 0.4999. This stress-state specification is material to the interpretation of the near-incompressible results: Cook's membrane is a plane-stress problem and is not an independent volumetric-locking test at $\nu = 0.4999$.

The plate-with-hole benchmark is a plane-strain quarter model with hole radius $a = 1$, outer extent $5a$, $E = 1000$, $\nu = 0.3$, and unit thickness. Symmetry imposes $u_y = 0$ on $y = 0$ and $u_x = 0$ on $x = 0$, and the hole boundary is traction-free. On $x = 5a$ and $y = 5a$, every formulation applies the traction vector obtained by multiplying the complete Kirsch stress tensor by the outward normal, evaluated at each boundary quadrature or collocation point. The outer loading is therefore the exact Kirsch traction, not a uniform remote-stress traction. Finite outer truncation does not create a boundary-data mismatch. The FEM and EFG domains approximate the circular hole by straight inner segments, so their near-hole deviations also contain geometry, differentiation, and stress-evaluation error; the DEM integration mapping retains the circular inner boundary.

The crack benchmark is a plane-strain quarter-domain model on $0 \le x \le 10a$ and $0 \le y \le 10a$, with $a = 1$. Symmetry imposes $u_x = 0$ on $x = 0$ and $u_y = 0$ on the ligament $y = 0$, $x \ge a$; the crack face $y = 0$, $x < a$ is traction-free. A uniform remote traction $t_y = \sigma$ is applied on $y = 10a$, and $x = 10a$ is traction-free. The comparison uses the nominal infinite-plate value $K_I = \sigma\sqrt{\pi a}$, which is not an exact solution for this finite domain.

The recorded numerical outputs comprise FEM and EFG displacement and energy errors for the cantilever; tip displacements for Cook's membrane; energy and hole-boundary stress errors for the plate with a hole; and stress-intensity-factor estimates for the crack. DEM outputs contain problem-specific displacement or energy errors, final training loss, wall-clock time, and trial-level data. Because no single metric is available for every method-problem pair, the reported cross-method comparisons use quantities available for all three formulations on the relevant problem.

3.1. Comparability of the reported errors

The same mathematical definitions are used for each reported quantity, but the bulk error integrals use each formulation's native integration rule. Two common-point checks assess the localized hole and crack quantities at the finest configurations. The near-hole check uses the same 256 angular midpoints on $r = 1.01a$. For the crack interaction integral, a 40×40, 80×80, and 160×160 Cartesian quadrature sequence is used with identical q-function, auxiliary fields, and half-domain factor for all three methods; the finest shared-grid values are reported. Cook's membrane is treated separately: all three benchmarked implementations are evaluated against a quadratic Q8 convergence sequence, so the Q4 results do not define their own comparison value. These procedures improve comparability without imposing one solver's native integration rule on the other formulations.

The horizontal coordinates used in the refinement and capacity figures are method-specific. FEM and EFG are indexed by nodal displacement unknowns, whereas DEM is indexed by trainable parameters. These coordinates are retained only for within-method refinement or capacity trends. Cross-method efficiency is assessed instead through error versus measured wall-clock time and the first tested configuration meeting a common accuracy threshold (Section 5.8 and Table 5). Memory use was not recorded and is not claimed as a comparison axis.

3.2. Refinement, timing, and stochastic trials

For FEM and EFG, an observed slope is obtained from a least-squares fit of $\log(\text{error})$ against $\log(N_{\text{dof}})$. For DEM, the corresponding slope describes variation with network parameter count and is reported separately because it is not an h-convergence rate.

Wall-clock values are obtained using an 11th Gen Intel® Core™ i7-1165G7 processor running at 2.80 GHz, with computation performed entirely on the CPU (no discrete, CUDA-capable GPU was used). These results are therefore used only to characterize the implementations tested here under these specific conditions, not to infer hardware-independent computational complexity.

DEM uses two independently seeded trials per width in the baseline runs. At $\nu = 0.4999$, five trials per width are available for both the cantilever and Cook's membrane. The pooled Spearman coefficient is reported as a descriptive ordering diagnostic. A separate sensitivity study fixes neural capacity near 2900 parameters and compares tanh architectures 2×51, 4×30, and 6×23 using five seeds each. Every run is evaluated after Adam and after the subsequent L-BFGS stage. This design quantifies depth and optimizer-stage sensitivity but is not a complete factorial separation of representation and optimization error.

4. Mathematical Formulation

4.1. Governing equations and variational principle

All three methods solve the same two-dimensional linear-elastostatic boundary value problem on a domain Ω with boundary $\partial\Omega = \Gamma_u \cup \Gamma_t$ ($\Gamma_u \cap \Gamma_t = \emptyset$):

$$\nabla \cdot \sigma + b = 0 \text{ in } \Omega, \quad \varepsilon = \nabla_s u \text{ in } \Omega, \quad \sigma = D\varepsilon \text{ in } \Omega,$$
$$u = \bar{u} \text{ on } \Gamma_u, \quad \sigma \cdot n = \bar{t} \text{ on } \Gamma_t, \tag{1}$$

with $\boldsymbol{\varepsilon} = [\varepsilon_{xx}, \varepsilon_{yy}, \gamma_{xy}]^T$, where $\gamma_{xy} = 2\varepsilon_{xy}$ is the engineering (as opposed to tensorial) shear strain, and the isotropic plane constitutive matrix, identical across every FEM/EFG/DEM driver in this project:

$$D_{stress} = \frac{E}{1-\nu^2}\begin{bmatrix} 1 & \nu & 0 \\ \nu & 1 & 0 \\ 0 & 0 & \frac{1-\nu}{2} \end{bmatrix}, \quad D_{strain} = \frac{E}{(1+\nu)(1-2\nu)}\begin{bmatrix} 1-\nu & \nu & 0 \\ \nu & 1-\nu & 0 \\ 0 & 0 & \frac{1-2\nu}{2} \end{bmatrix}. \tag{2}$$

The three methods are unified by a single variational statement: the total potential energy functional:

$$\Pi[u] = \frac{1}{2}\int_\Omega \varepsilon(u)^T \quad D\,\varepsilon(u)\, d\Omega \qquad - \int_\Omega b \cdot u \, d\Omega \quad - \int_{\Gamma_t} \bar{t} \cdot u \, d\Gamma, \quad u = \bar{u} \text{ on } \Gamma_u. \tag{3}$$

For linear elasticity, the continuum functional is quadratic and convex in the admissible displacement field. The exactly constrained FEM discretization seeks its stationary point in a bilinear finite-dimensional space. EFG uses the same interior bilinear form but, in this implementation, adds a finite essential-boundary penalty and therefore solves a penalty-augmented discrete problem. DEM substitutes a neural-network trial function and minimizes a numerically integrated objective that may also contain a soft boundary penalty. Thus, the continuum energy is common, whereas the discrete admissible sets, quadrature rules, and constraint treatments are formulation-specific. Figure 3 contrasts how each method discretizes Ω to represent this shared trial space: a conforming element mesh (FEM), a scattered node cloud with overlapping MLS support domains and an independent background integration grid (EFG), and sparse collocation points feeding a continuous neural-network trial field (DEM).

Explicitly, setting $\delta\Pi = 0$ for admissible variations $\delta\boldsymbol{u}$ vanishing on Γ_u gives the weak (virtual-work) form:

$$\int_\Omega \varepsilon(\delta u)^T D \;\; \varepsilon(u)\, d\Omega = \int_\Omega \delta u \cdot b \, d\Omega + \int_{\Gamma_t} \delta u \cdot \; \bar{t} \, d\Gamma, \quad \forall\, \delta u \in V_0, \tag{4}$$

with $V_0 = \{\boldsymbol{v} \in H^1(\Omega) : \boldsymbol{v} = \boldsymbol{0} \text{ on } \Gamma_u\}$. Substituting a Galerkin trial expansion $\boldsymbol{u}^h(\boldsymbol{x}) = \Sigma_I \, N_I(\boldsymbol{x})\, \boldsymbol{d}_I$ (shape functions N_I, nodal unknowns $\boldsymbol{d}_I$) and the matching test-function expansion into Eq. (4) gives the discrete system referenced throughout this section:

$$Kd = F, \quad K = \int_\Omega B^T D B \, d\Omega, \quad F = \int_\Omega N^T b \, d\Omega + \int_{\Gamma_t} N^T \bar{t} \;\; d\Gamma, \tag{5}$$

where $\boldsymbol{B} = \nabla_s \boldsymbol{N}$ collects shape-function derivatives into the standard strain-displacement operator. Equation (5) is identical in form for FEM and EFG; the two methods differ only in the choice of N_I: FEM's compactly-supported, element-based, interpolatory shape functions versus EFG's support-radius-limited, non-interpolatory moving-least-squares φ_I (Sections 4.3-4.4).

4.2. Error measures and theoretical expectations

For a computed field $\boldsymbol{u}^h$ and a reference field $\boldsymbol{u}$, the displacement L_2 error and energy error are:

$$\|u^h - u\|_{L_2(\Omega)} = \left(\int_\Omega \|u^h - u\|^2 \, d\Omega\right)^{1/2}, \tag{6}$$

$$\|u^h - u\|_{E(\Omega)} = \left(\frac{1}{2}\int_\Omega (\varepsilon^h - \varepsilon)^T \quad D(\varepsilon^h - \varepsilon)\, d\Omega\right)^{1/2}. \tag{7}$$

For a conforming Galerkin space with exact essential constraints and exact integration, the Ritz solution is the best approximation in the induced energy norm. The present computations depart from that ideal in different ways: isoparametric and background quadrature are numerical, and EFG uses a finite penalty rather than an exactly constrained admissible space. The classical best-approximation statement is therefore used as theoretical context for FEM/EFG, not as an exact identity for every computed result. This distinction is important when interpreting the EFG patch-test floor.

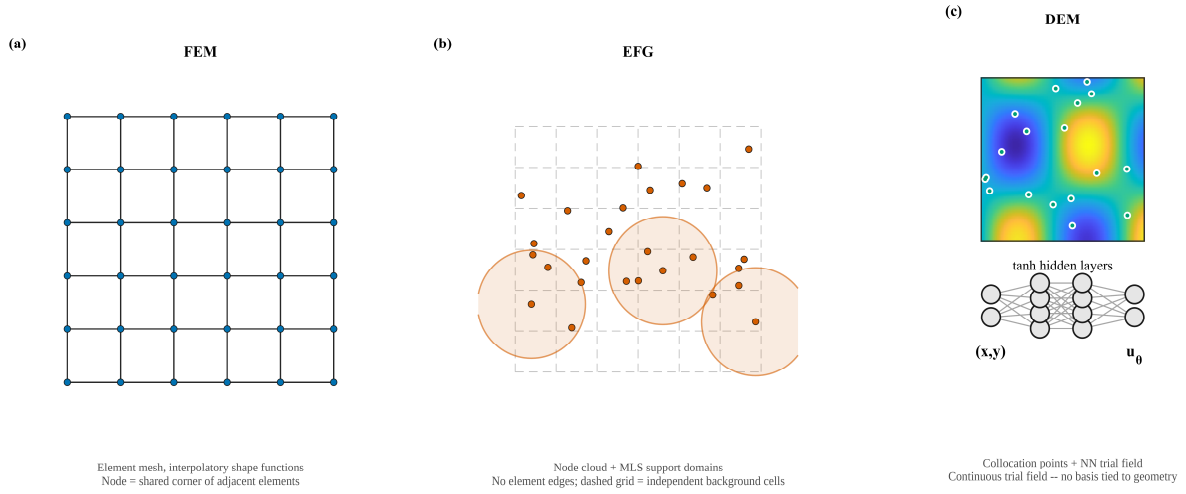


Fig. 3. How each method discretizes the domain: (a) element mesh (FEM), (b) node cloud with MLS support domains (EFG), and (c) collocation points with a neural-network trial field (DEM).

For a complete polynomial approximation of order p on a quasi-uniform discretization of size h, with sufficient solution regularity, standard interpolation theory gives:

$$\|u - u^h\|_{E(\Omega)} \;\leq\; C\; h^p\; |u|_{H^{p+1}(\Omega)}. \tag{8}$$

In two dimensions, $N_{\text{dof}} \sim h^{-2}$, so a first-order approximation is expected to show an energy-error slope near 0.5 against nodal degrees of freedom in a smooth asymptotic regime. This expectation applies naturally to the smooth cantilever solution. A circular hole has a smooth boundary and the Kirsch field has a finite stress concentration; it is not a re-entrant-corner or crack-tip singularity. Reduced rates on the hole problem must therefore be investigated in terms of curved-geometry approximation, finite-domain effects, stress recovery, quadrature, and pre-asymptotic refinement rather than attributed to a nonexistent loss of regularity. The crack is different: the Williams field has displacement behavior $r^{1/2}$ and stress behavior $r^{-1/2}$, so the regularity required for the first-order smooth estimate fails at the tip [63].

4.3. Finite element method

Ω is partitioned into 4-node bilinear quadrilateral (Q4) elements. Both geometry and displacement are interpolated isoparametrically by bilinear shape functions on the parent domain $(\xi, \eta) \in [-1,1]^2$:

$$N_a(\xi,\eta) \;=\; \frac{1}{4}(1+\xi_a\xi)(1+\eta_a\eta), \quad a = 1,\dots,4, \tag{9}$$

with $(\xi_a, \eta_a) \in \{(-1,-1),(1,-1),(1,1),(-1,1)\}$. Crucially, $N_a(\boldsymbol{x}_b) = \delta_{ab}$: Q4 shape functions are interpolatory - the property that lets FEM enforce Dirichlet BCs exactly by direct nodal substitution, and a key point of contrast with EFG below. Physical-space derivatives follow from the isoparametric Jacobian, $\nabla_x N_a \;=\; \boldsymbol{J}^{-1}\,\nabla_{\xi\eta} N_a$, populating Eq. (5)'s strain-displacement operator [64, 65] for a single Q4 element (3×8, one column-pair per node):

$$B_e \;=\; \begin{bmatrix} N_{1,x} & 0 & N_{2,x} & 0 & N_{3,x} & 0 & N_{4,x} & 0 \\ 0 & N_{1,y} & 0 & N_{2,y} & 0 & N_{3,y} & 0 & N_{4,y} \\ N_{1,y} & N_{1,x} & N_{2,y} & N_{2,x} & N_{3,y} & N_{3,x} & N_{4,y} & N_{4,x} \end{bmatrix}, \tag{10}$$

and the element stiffness is Eq. (5)'s integral restricted to one element, evaluated by full 2×2 Gauss-Legendre quadrature:

$$K_e \;=\; t \sum_{q=1}^{4}\; B_e(\xi_q,\eta_q)^T D\;\; B_e(\xi_q,\eta_q)\; detJ(\xi_q,\eta_q)\; w_q. \tag{11}$$

Element matrices are scattered into the global sparse stiffness $\boldsymbol{K}$ by standard connectivity mapping. Essential (Dirichlet) BCs are enforced exactly, by partitioning free/prescribed DOFs and eliminating the prescribed ones:

$$K_{ff}\; d_f \;=\; F_f \;-\; K_{fp}\; \bar{d}_p, \quad d_p \;=\; \bar{d}_p, \tag{12}$$

with no penalty parameter to tune. With the quadrature scheme and boundary data used here, this exact enforcement is consistent with the machine-precision FEM patch result, whereas the finite-penalty EFG result exhibits a nonzero floor (Section 5.2).

4.4. Element-free Galerkin method

EFG [1,66] solves the identical strong and weak forms but replaces the mesh with a scattered cloud of N nodes x_I ($I = 1,\dots,N$) and Moving-Least-Squares (MLS) [67] shape functions, with no element connectivity defining the trial space. The EFG framework supports arbitrary-order MLS polynomial bases; this study uses a complete linear basis. At an evaluation point x, a local weighted least-squares fit of $p(x) = [1, x, y]^T$ is constructed from the nodes whose supports contain x:

$$A(x) \;=\; \sum_I\; w_I(x)\; p(x_I)p(x_I)^T, \quad \gamma(x) \;=\; A(x)^{-1}p(x), \quad \varphi_I(x) \;=\; \gamma(x)^T\; w_I(x)\; p(x_I). \tag{13}$$

The weight function $w_I(\boldsymbol{x}) \;=\; w(r_I)$, $r_I \;=\; |\boldsymbol{x} - \boldsymbol{x}_I|/d_I$ (d_I: nodal support radius), uses the standard cubic spline [3]:

$$w(r) \;=\; \begin{cases} \dfrac{2}{3} \;-\; 4r^2 \;+\; 4r^3, & r \leq \dfrac{1}{2} \\[2ex] \dfrac{4}{3} \;-\; 4r \;+\; 4r^2 \;-\; \dfrac{4}{3}r^3, & \dfrac{1}{2} < r \leq 1 \\[2ex] 0, & r > 1. \end{cases} \tag{14}$$

By construction, the MLS approximation inherits the completeness of its basis: for any $\boldsymbol{x}$ whose support contains at least $m = \dim\boldsymbol{p}$ non-degenerate nodes, the shape functions of Eq. (13) satisfy the reproducing (consistency) conditions [68, 69]:

$$\sum_I\; \varphi_I(x)\; p(x_I) \;=\; p(x) \quad\Longleftrightarrow\quad \sum_I\; \varphi_I \;=\; 1, \quad \sum_I\; \varphi_I\; x_I \;=\; x, \quad \sum_I\; \varphi_I\; y_I \;=\; y, \tag{15}$$

for the first-order basis used here. Equation (15) states that EFG reproduces any linear displacement field exactly in the domain interior, and is the formal reason EFG satisfies the patch test's consistency requirement (Section 5.2) up to the accuracy with which essential boundary conditions are imposed -- isolating the penalty enforcement of Eq. (17), not the approximation space, as the sole source of the residual patch-test error reported there. Equation (15) also makes the method's conditioning requirement explicit: it holds only while $\boldsymbol{A}(\boldsymbol{x})$ remains invertible, which fails if fewer than m nodes influence $\boldsymbol{x}$ or if the influencing nodes become collinear. This invertibility requirement sets the practical minimum admissible support radius.

Critically, $\varphi_I(\boldsymbol{x}_J) \neq \delta_{IJ}$ in general: EFG's shape functions are non-interpolatory, so the nodal "displacements" $\boldsymbol{d}_I$ are not the physical displacement at $\boldsymbol{x}_I$. This has two consequences documented throughout Section 5: essential BCs cannot be enforced by nodal substitution, and downstream error/energy computations must always evaluate $\boldsymbol{u}^h$ at genuine field points, never read off nodal values. Figure 4 visualizes this: nodes' overlapping, non-interpolatory support domains and a representative MLS shape function, contrasted directly against FEM's compactly-supported, interpolatory hat function from the previous subsection.

Differentiating Eqs. (13) (product rule through $\boldsymbol{A}^{-1}$) gives the shape-function gradients that populate $\boldsymbol{B}$ in Eq. (5):

$$\gamma_{,i}(x) \;=\; A(x)^{-1}(p_{,i}(x) \;-\; A_{,i}(x)\;\gamma(x)), \quad \varphi_{I,i}(x) \;=\; \gamma_{,i}(x)^T\; w_I(x)p(x_I) \;+\; \gamma(x)^T\; w_{I,i}(x)\; p(x_I), \qquad i = x, y, \tag{16}$$

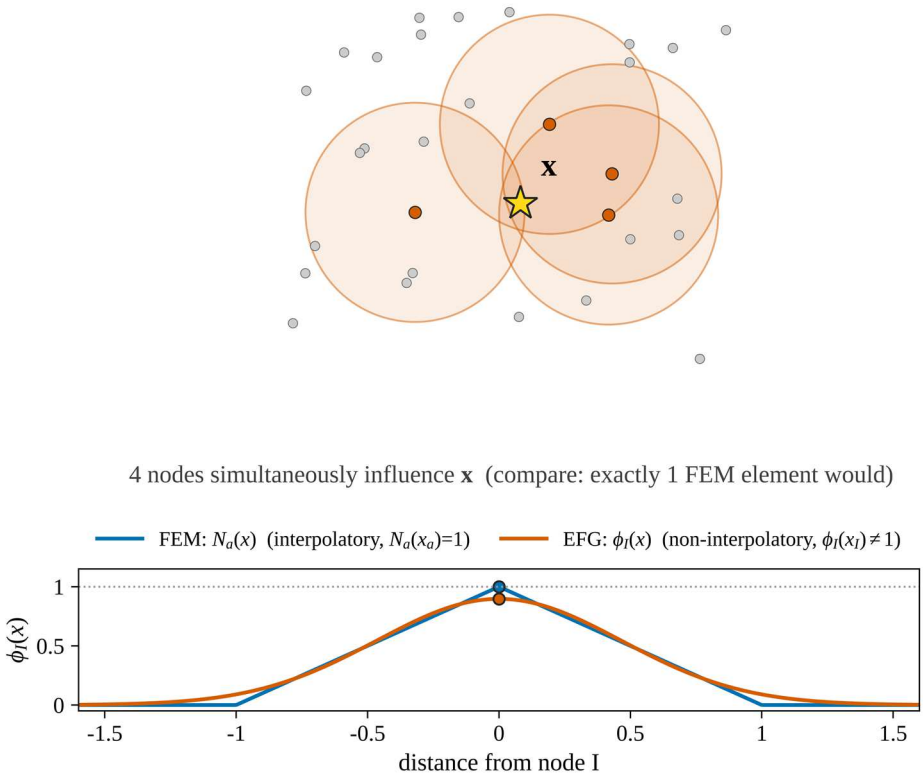


Fig. 4. EFG's overlapping, non-interpolatory MLS influence domains, contrasted against FEM's interpolatory hat function.

with $\boldsymbol{A}_{,i}(\boldsymbol{x}) = \Sigma_I \; w_{I,i}(\boldsymbol{x}) \; \boldsymbol{p}(\boldsymbol{x}_I) \; \boldsymbol{p}(\boldsymbol{x}_I)^T$. Unlike FEM's shape-function derivatives, which follow directly from a fixed polynomial via the isoparametric Jacobian, Eq. (16) requires differentiating through the moment-matrix inverse at every evaluation point, a standard but easy-to-mis-implement step [1]. A direct (non-vectorized) implementation of this step is prohibitively slow at the point densities this study's finer benchmark levels require; the results reported here use a vectorized matrix-form implementation instead.

Away from Γ_u, EFG's interior stiffness and force vectors follow Eq. (5) exactly, with $\boldsymbol{B}$ built from $\nabla\varphi_I$ Eq. (16) in place of FEM's $\nabla\, N_a$. Because φ_I has no fixed relationship to any element, this integral is instead evaluated over an independent, regular background grid of quadrature cells (a finer $4 \times 4 = 16$-point rule per cell here, versus FEM's $2 \times 2 = 4$, since φ_I is rational, not polynomial), summing at each Gauss point the contribution of whichever nodes' support currently covers it. Essential BCs, which cannot be imposed by direct substitution given $\varphi_I(\boldsymbol{x}_J) \neq \delta_{IJ}$, are instead enforced weakly via the penalty method, added on top of this same interior $\boldsymbol{K}$:

$$K \mathrel{+}= \alpha \int_{\Gamma_u} \varphi\varphi^T \, d\Gamma, \quad F \mathrel{+}= \alpha \int_{\Gamma_u} \varphi \; \bar{u} \, d\Gamma, \tag{17}$$

The penalty is $\alpha = 10^5 E$ for the patch test. For the cantilever, Cook's membrane, and plate-with-hole problems, $\alpha = 10^3 K_{\text{scale}}$, where K_{scale} is the largest absolute assembled stiffness entry before the boundary penalty. For the crack, $\alpha = 10 K_{\text{scale}}$ is used because larger global penalties caused severe conditioning on the graded support distribution. Equation (17) is the stationarity condition of the total potential energy augmented by $\alpha/2$ times the boundary integral of $|u - \bar{u}|^2$ over Γ_u. The constraint is recovered only as $\alpha \to \infty$, while conditioning deteriorates as α increases. Alternative Lagrange-multiplier, transformation, or boundary-kernel treatments [70–72] are outside the fixed-formulation comparison.

The support radii are fixed by problem: $d_I = 3.5h$ for the patch test; $2.0\max(\Delta x, \Delta y)$ for the cantilever; $2.5(60/n)$ for Cook's membrane; $2.5(4/n_r)$ for the plate with a hole; and 1.8 times the largest local neighbor distance, capped at $0.6W$, for the graded crack cloud. The EFG node/background-cell counts are 36/400 (patch); 147/96, 485/384, and 1737/1536 (cantilever); 81/64, 289/256, and 625/576 (Cook); 91/72, 231/200, and 561/512 (hole); and 231/200 and 561/512 (crack). Each background cell uses 4×4 Gauss points.

4.5. Deep energy method

DEM [2] solves the same variational statement Eq. (3) by direct numerical minimization over a neural-network trial function, a choice justified in principle by the universal approximation theorem [73,74,75,76], which guarantees a sufficiently wide feedforward network can approximate any continuous function to arbitrary accuracy, though it says nothing about whether gradient-based training will actually find such a network in practice. Quantitative error bounds for this class of method, analogous to Eq. (8) for Galerkin discretizations, remain an active area and are currently available only under assumptions on the trained network's generalization behaviour [77]; no such bound is invoked here, and DEM's accuracy is assessed purely empirically against the same references used for FEM and EFG. The network $\boldsymbol{u}_\theta : R^2 \to R^2$ is fully-connected and feedforward: 2 inputs (x, y), L hidden layers of width n with tanh activation, 2 outputs (u_x, u_y). Its trainable parameter count follows directly from the layer sizes:

$$P(n, L) \;=\; 3n_{2\to\, n} \;+\; (L-1)(n^2+n)_{\text{hidden-to-hidden}} \;+\; (2n+2)_{n\to 2} \quad =\; 5n + 2 + (L-1)(n^2+n), \tag{18}$$

For example, $P(15{,}4) = 797$ and $P(45{,}4) = 6437$ for the smallest and largest networks tested. In the Results, P is reported as the trainable parameter count and is not called a neural degree-of-freedom count. It is a capacity descriptor rather than a measure equivalent to FEM or EFG nodal resolution, so it is used only for within-DEM trends and is not interpreted as a like-for-like measure of resolution or computational cost.

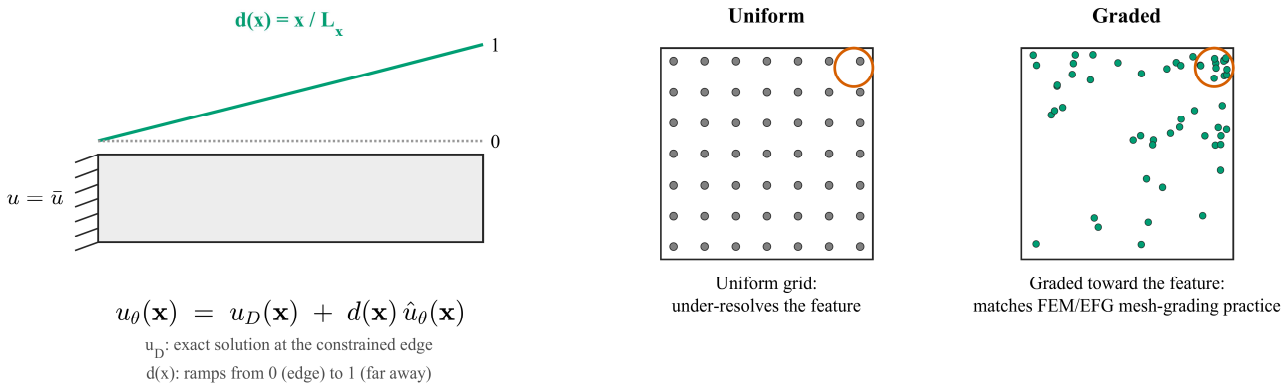


Fig. 5. DEM's hard-constraint ansatz Eq. (19) and uniform-vs-graded collocation-point distributions near a stress concentration.

The network is evaluated on normalized coordinates $\xi = x/L_x$ and $\eta = y/L_y$, and its raw output is rescaled by a problem-specific reference displacement U_{ref} (for the cantilever, $U_{\text{ref}} = 4PL^3/(ED^3)$). Without this non-dimensionalization, the network's $O(1)$ output scale differs substantially from the physical displacement scale and yields an ill-conditioned optimization problem. Where the essential boundary is geometrically simple, the Dirichlet condition is imposed exactly through a hard-constraint ansatz originating from early neural-network PDE solvers [78]:

$$u_\theta(x) \;=\; u_D(x) \;+\; d(x)\;\hat{u}_\theta(x), \quad d(x) \;=\; \xi \;=\; x/L_x, \tag{19}$$

where $\boldsymbol{u}_D$ is the prescribed Dirichlet data and $d(\boldsymbol{x})$ vanishes exactly on Γ_u. Where a closed-form $d(\boldsymbol{x})$ is impractical (e.g., the patch test's all-edge constraint), a soft penalty $P(\theta) = (1)/(N_{\text{bc}})\Sigma_k|\boldsymbol{u}_\theta(\boldsymbol{x}_k) - \bar{\boldsymbol{u}}(\boldsymbol{x}_k)|^2$ is used instead, weighted by β in the loss. Figure 5 illustrates this ansatz, and also contrasts the uniform collocation-point distribution used away from any stress concentration against the graded distribution used near one (the plate-hole boundary and the crack tip) -- matching FEM/EFG's own mesh-grading practice at the same locations.

The training loss is Eq. (3) evaluated at fixed interior collocation points and boundary traction points with quadrature weights from a background integration grid:

$$L(\theta) \;=\; t\sum_j \frac{1}{2}\varepsilon(u_\theta(x_j))^T\; D\;\varepsilon(u_\theta(x_j))\;w_j \qquad - \;\; t\sum_k \;\bar{t}(x_k)\cdot u_\theta(x_k)\;w_k \;\;+\;\; \beta\;P(\theta), \tag{20}$$

with strains $\boldsymbol{\varepsilon}(\boldsymbol{u}_\theta) = \nabla_s \boldsymbol{u}_\theta$ obtained by automatic differentiation [79], not shape-function derivatives -- only the trial function's strain-level derivatives are required, markedly cheaper than the higher-order derivatives a strong-form collocation PINN loss needs [10].

Because $L(\theta)$ is non-convex in θ, training uses Adam [80,81] with learning rate 0.005 and gradient-norm clipping at $|\nabla L| = 10$, followed by a custom L-BFGS refinement [82–84] with Armijo backtracking and history size 10. The baseline budget scales linearly with network width ($n = 30$ gives 3000 Adam epochs and 800 L-BFGS iterations). Independently seeded trials are retained individually; the lowest-final-loss trial supplies the headline DEM value, and Section 5.7 audits whether that selection also minimizes the engineering error.

The fixed DEM integration sets contain 1600, 2304, 4096, 4096, and 12,288 interior points for the patch, cantilever, Cook, hole, and crack problems, respectively. Boundary sets contain 160 prescribed-displacement points for the patch; 32 traction points for the cantilever; 32 traction points for Cook; 80 outer-traction points for the hole; and 48 top-traction plus 48 ligament-penalty points for the crack. These counts are held fixed across the width sweep. The corresponding FEM node/cell sequences are 147/96, 485/384, 1737/1536, and 6545/6144 (cantilever); 25/16, 81/64, 289/256, 1089/1024, and 2401/2304 (Cook); 45/32, 153/128, 561/512, and 2145/2048 (hole); and 325/288, 861/800, and 2145/2048 (crack).

Two structural facts about $L(\theta) = \Pi[\boldsymbol{u}_\theta]$ are relevant to the training audit. First, although $\Pi[\boldsymbol{u}]$ is quadratic and convex as a functional of the displacement field, the composed objective is generally non-convex in the network parameters. Consequently, optimization failure and seed dependence can occur even though the underlying linear-elastic boundary-value problem has a unique solution.

Second, when essential data are imposed exactly and homogeneously, no body force is present, and the applied traction performs positive work, Clapeyron's theorem gives

$$\Pi[u^*] \;=\; -\frac{1}{2}\int_{\Gamma_t} \bar{t}\cdot u^*\; d\Gamma \;<\; 0. \tag{21}$$

The sign is therefore a necessary consistency check for the hard-constrained Cook and plate-with-hole runs, but it is not a convergence certificate. Quadrature changes the numerical objective, the crack includes a penalty constraint, and the patch and cantilever use boundary constructions for which the homogeneous formula does not apply. The six non-finite attempts and inverse loss-error ordering of the finite trials provide the evidence for training instability in the near-incompressible cantilever; the sign of the final loss is not used for that classification.

5. Results

5.1. Headline accuracy

Table 3 reports the finest deterministic FEM and EFG values and the lowest-final-loss DEM value at the largest tested width, unless otherwise stated. Thus the 77.54% near-incompressible cantilever entry is loss-selected, not the minimum engineering error among all finite trials. Cook's membrane errors use the independent finest Q8 references, 8.368995×10^{-3} at $\nu = 0.3$ and 8.467516×10^{-3} at $\nu = 0.4999$. The values are not expected outcomes over random seeds and do not equate the computational resolution of nodal and neural representations.

Table 3. Reported accuracy for the tested formulations. FEM and EFG entries use the finest listed spatial discretization; DEM entries use the lowest-final-loss trial at the largest listed width. Energy entries are relative energy-norm errors normalized by the exact energy norm. Cook uses the independent Q8 reference; the hole and crack localized rows use the shared post-processing checks.

Problem	Metric	FEM	EFG	DEM
Patch test	Displacement error, prescribed linear field	$\sim 10^{-18}$	2×10^{-3}	$1.5 - -3\%$
Cantilever, $\nu = 0.3$	Tip displacement	0.63%	0.010%	0.39%
Cantilever, $\nu = 0.4999$	Tip displacement	80.36%	0.33%	77.54%
Cantilever, $\nu = 0.3$	Energy-norm error	7.94%	0.77%	15.95%
Cantilever, $\nu = 0.4999$	Energy-norm error	97.94%	6.60%	136.10%
Cook, $\nu = 0.3$	Tip displacement	0.71%	0.26%	0.93%
Cook, $\nu = 0.4999$	Tip displacement	0.81%	0.31%	0.84%
Plate with hole	Energy error	2.292×10^{-3}	2.113×10^{-3}	5.577×10^{-3}
Plate with hole	Shared $r = 1.01a$ maximum σ_x error	11.60%	12.48%	18.36%
Center crack	Shared-grid $\lvert K_I \rvert$ deviation (160×160)	0.33%	9.02%	73.13%

5.2. Patch test

The patch test checks reproduction of a constant-strain field [85]. The FEM result obtained here is at machine precision. The EFG result exhibits a nonzero floor as the penalty is increased, consistent with exact linear MLS reproduction in the interior but approximate essential-boundary enforcement. Because numerical integration and conditioning are also present, the data support "penalty-dominated residual" more strongly than the claim that every component of the residual has been isolated. DEM enforces the all-edge displacement data by a soft penalty and returns a small but nonzero displacement error. It should therefore be interpreted as a consistency check for this trained formulation, not as an exact patch-test pass.

5.3. Cantilever beam

At $\nu = 0.3$, the finest FEM, EFG, and DEM tip-displacement errors are 0.63%, 0.010%, and 0.39%, respectively. FEM and EFG improve monotonically under spatial refinement. The selected DEM errors also decrease over the four widths, although a width sweep combines representation and stochastic optimization and is not a classical discretization sequence.

At $\nu = 0.4999$, full-integration Q4 FEM is strongly over-stiff: its finest tip displacement is 19.64% of the reference, corresponding to an 80.36% error. The tested EFG formulation improves from a 32.40% error on its coarsest node set to 0.33% on the finest set. This result demonstrates reduced locking for the tested EFG configuration; it does not establish locking-free behavior for all EFG formulations, which depends on support, integration, and formulation choices [22, 23].

DEM remains inaccurate in this plane-strain cantilever case. Six of twenty attempts return non-finite values. Among the fourteen finite trials, the lowest-loss trial has the largest tip-displacement error at every width, and the pooled Spearman diagnostic is $\rho = -0.92$. These results identify optimization instability for the tested architecture and schedule, but do not isolate its cause. Cook's membrane cannot be used to rule out volumetric effects because it is analyzed in plane stress. The contrast instead shows problem dependence across two different stress states and leaves plane-strain volumetric conditioning, bending kinematics, boundary construction, and optimizer conditioning entangled. Figure 6 reports a consistently normalized relative energy error. At $\nu = 0.3$, the finest errors are 7.94% (FEM), 0.77% (EFG), and 15.95% (loss-selected DEM). At $\nu = 0.4999$, they are 97.94%, 6.60%, and 136.10%, respectively.

Cook's membrane has no closed-form solution [86]. The independent finest Q8 values are used as the common numerical references. At $\nu = 0.3$, the finest Q4 FEM, EFG, and DEM deviations are 0.71%, 0.26%, and 0.93%. At $\nu = 0.4999$, the corresponding deviations are 0.81%, 0.31%, and 0.84%. All three implementations therefore reach below 1% at their finest tested configurations without defining the reference through one of the compared Q4 results.

5.4. Cook's membrane

Unlike the near-incompressible cantilever, all sampled $\nu = 0.4999$ Cook DEM runs remain finite in the baseline width sweep, and the largest-width error relative to the independent Q8 reference is 0.84%. The contrast confirms that the observed DEM difficulty is problem-dependent within the present suite. It does not isolate whether bending kinematics, volumetric conditioning, geometry, constraint construction, or optimization is dominant.

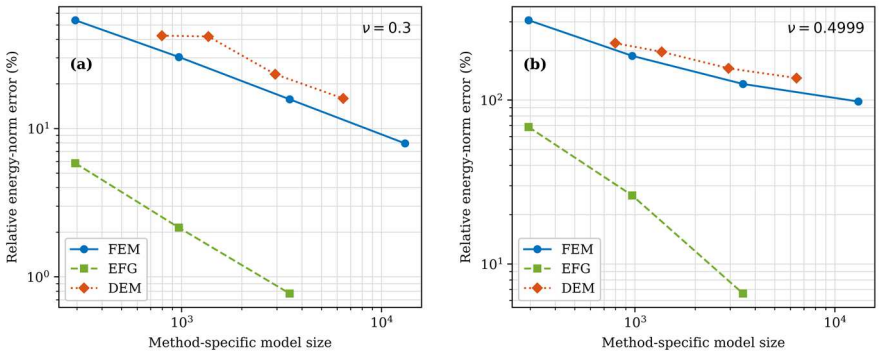


Fig. 6. Cantilever relative energy-norm error. FEM and EFG use direct strain-error integration and DEM uses $\sqrt{\Pi[u^h] - \Pi[u]}$ for the hard-admissible cantilever trial; all are divided by the exact energy norm. At the finest tested configurations, (a) the errors are 7.94% (FEM), 0.77% (EFG), and 15.95% (DEM) at $\nu = 0.3$, and (b) 97.94% (FEM), 6.60% (EFG), and 136.10% (DEM) at $\nu = 0.4999$. FEM and EFG are indexed by nodal displacement unknowns; DEM is indexed by trainable parameters, so horizontal positions are not resolution-equivalent.

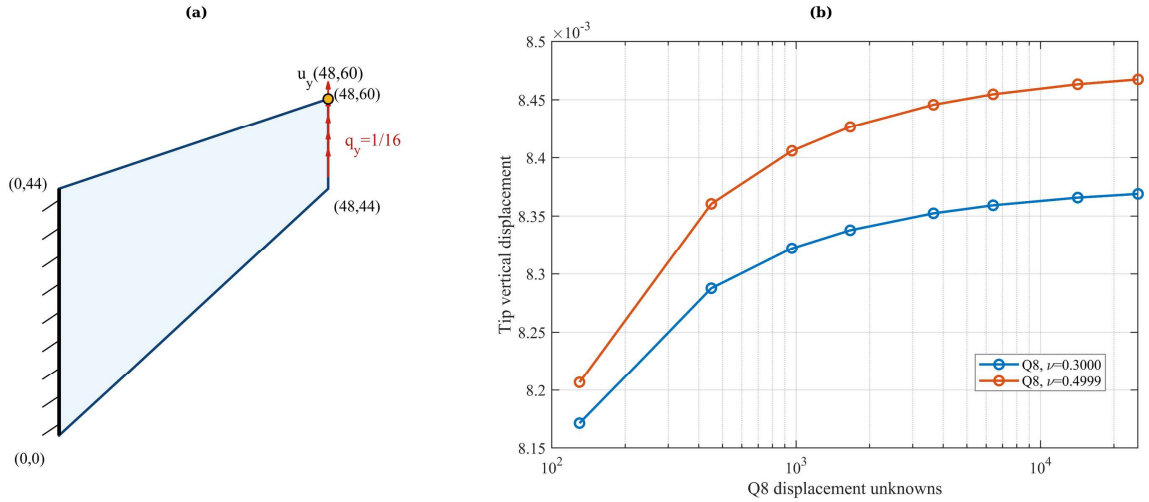


Fig. 7. Cook's membrane verification: (a) Geometry, boundary conditions, loading, and reported tip quantity, (b) Independent Q8 reference sequence. At 25,090 Q8 displacement unknowns, $u_y(48,60) = 8.368995 \times 10^{-3}$ for $\nu = 0.3$ and 8.467516×10^{-3} for $\nu = 0.4999$; the changes from the preceding Q8 level are 0.0379% and 0.0490%, respectively.

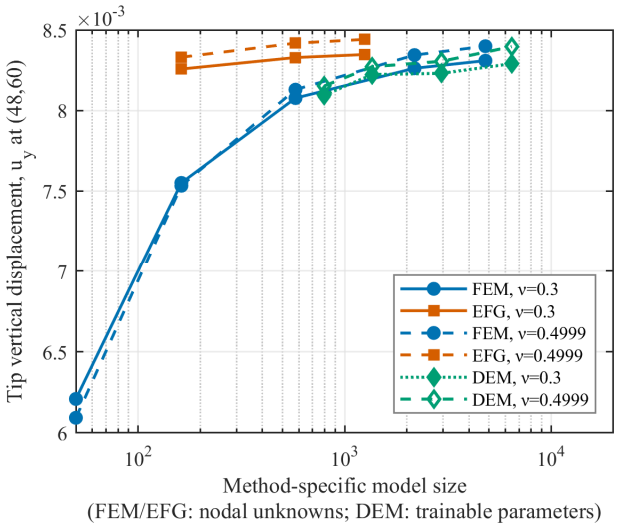


Fig. 8. Cook's membrane tip displacement versus each formulation's own refinement or capacity variable. The independent finest Q8 values are 8.368995×10^{-3} at $\nu = 0.3$ and 8.467516×10^{-3} at $\nu = 0.4999$. At the finest tested configurations, FEM, EFG, and DEM errors are 0.71%, 0.26%, and 0.93% for $\nu = 0.3$ and 0.81%, 0.31%, and 0.84% for $\nu = 0.4999$. Horizontal positions across nodal and neural representations are not resolution-equivalent.

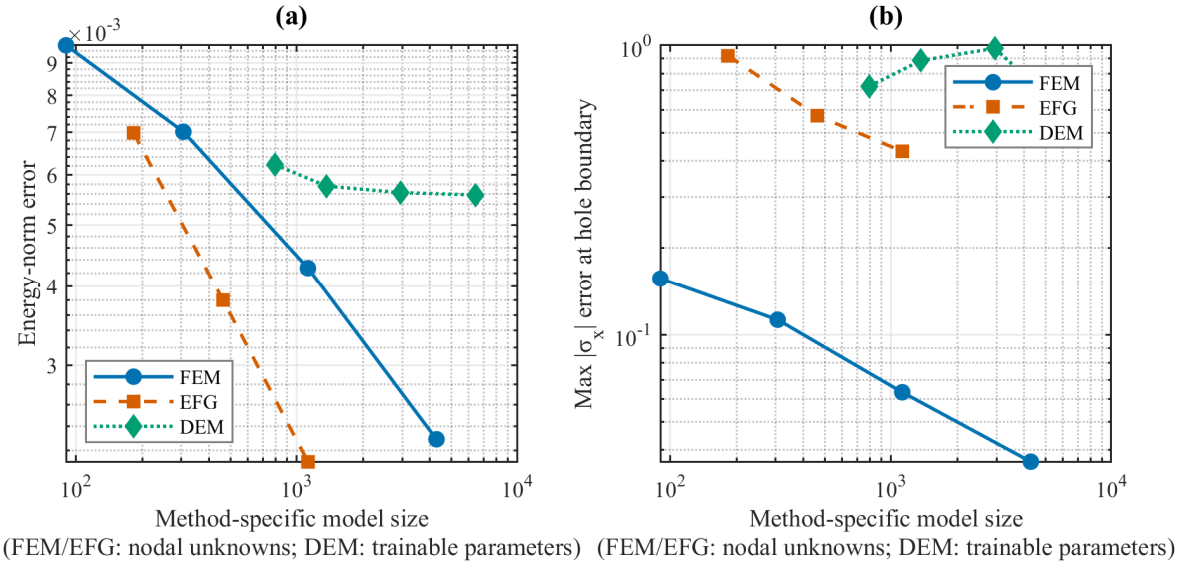


Fig. 9. Plate with a circular hole: bulk energy error and native maximum hole-boundary stress error. Each method is shown against its own refinement or capacity variable. At the finest tested spatial discretizations and loss-selected largest DEM width, the energy errors are 2.292×10^{-3} (FEM), 2.113×10^{-3} (EFG), and 5.577×10^{-3} (DEM), while the native trace maxima are 3.65% (FEM), 43.18% (EFG), and 56.78% (DEM). These native sampling sets are not resolution-matched; the common-ring comparison is reported in the text and Table 3.

5.5. Plate with a circular hole

The plate-with-hole benchmark distinguishes a bulk measure from a localized quantity of interest. The finest energy errors are 2.292×10^{-3}, 2.113×10^{-3}, and 5.577×10^{-3} for FEM, EFG, and DEM. The native boundary-trace maxima are 3.65%, 43.18%, and 56.78%, but they occur on different sampling sets and should not be read as a direct ranking. On the same 256 angular midpoints of the near-boundary ring $r = 1.01a$, the maximum errors normalized by the maximum exact $|\sigma_x|$ are 11.60% (FEM), 12.48% (EFG), and 18.36% (DEM); normalized RMSE values are 0.1838, 0.1925, and 0.2898. FEM and EFG are therefore close on the shared ring, and both are below DEM for this check. Because the exact Kirsch traction is applied on both finite outer edges, these values do not indicate an outer-boundary loading mismatch. The offset ring remains inside the chordal Q4 domain and is not a substitute for the exact boundary trace. The rise of the FEM value from 3.65% on its native trace to 11.60% on the shared ring instead confirms that evaluation location, chordal geometry, differentiation, and stress recovery materially affect the reported local error.

The circular boundary is smooth and the Kirsch stress concentration is finite. The reduced local accuracy cannot be attributed to a crack-like singularity or a re-entrant corner. Plausible contributors include curved-boundary geometry representation, local quadrature density, stress recovery, finite-domain truncation, EFG support and boundary treatment, and DEM's representation/optimization of steep local gradients. The current data do not provide an ablation that isolates these factors.

This problem also illustrates quantity-of-interest dependence in DEM trial selection. Final loss perfectly orders the eight sampled trials by energy error ($\rho = 1.00$), but has little association with the hole-boundary stress error ($\rho = 0.29$). Minimizing an integrated energy objective can therefore select an accurate bulk field without reliably selecting the best localized stress among nearby trained solutions. Figure 9 plots both the bulk energy error and the hole-boundary stress error against each formulation's own refinement or capacity variable.

5.6. Crack problem

The crack benchmark uses $K_I = \sigma\sqrt{\pi a}$ as a nominal infinite-plate normalization, not as exact ground truth for the finite square. Native-quadrature absolute deviations are 0.38% (FEM), 10.04% (EFG), and 73.06% (DEM). Under shared Cartesian interaction-integral quadrature, the signed FEM deviations at 40×40, 80×80, and 160×160 are -2.24%, -0.46%, and $+0.33\%$; the corresponding EFG deviations are -9.35%, -9.16%, and -9.02%, and the DEM deviations are -73.06%, -73.12%, and -73.13%. The 40-grid FEM sign change is therefore a post-processing-resolution effect. At 160×160, the common-grid absolute deviations are 0.33%, 9.02%, and 73.13%, preserving the native ordering while demonstrating that the comparison must state its extraction resolution.

The FEM value is extracted with a domain-form interaction integral and a conforming graded mesh. EFG uses the same type of extraction but only two refinement levels tested, so its fitted slope is not a well-conditioned convergence estimate. Its error is consistent with the known sensitivity of unenriched MLS fracture calculations to support grading, integration, and essential-boundary treatment, but the current results contain no condition-number data or alternative constraint formulation that would prove one dominant cause. Enriched EFG formulations are established remedies for crack-tip fields [87].

The unenriched tanh DEM returns a nearly width-independent K_I error. Smooth networks do not encode the Williams asymptotic field explicitly, and localized singular quantities can remain weakly coupled to the bulk energy objective. Similar final losses across widths neither establish that the global optimum of each network class was reached nor separate representation error from optimization error. Singular enrichment, local architectures, adaptive quadrature, mixed stress-displacement outputs, or alternative activations would be required to test the mechanism directly. The reported error therefore characterizes this unenriched tanh DEM configuration on the crack benchmark and does not define a performance limit for energy-based learning. Figure 10 plots stress-intensity error against each formulation's refinement or capacity variable. The cantilever sensitivity study demonstrates architecture and optimizer-stage dependence for that case but does not separate those effects for the crack field.

5.7. Reliability of DEM trial selection

Table 4 audits whether the lowest final training loss identifies the lowest error among the sampled trials at each width. "Agreement" counts width configurations for which the two choices coincide. The table also gives the finite-trial error range pooled across the tested widths to expose observed trial variability. These ranges and the pooled Spearman values are descriptive because widths are different capacity settings and the trials are too few for population-level inference.

The trial audit does not support a universal loss-based selection rule. Final loss orders some sampled bulk quantities, has weak association with the localized quantities, and is inversely ordered with the near-incompressible cantilever tip error. Reporting only the minimum-loss run omits non-finite outcomes and the observed trial-to-trial error variation.

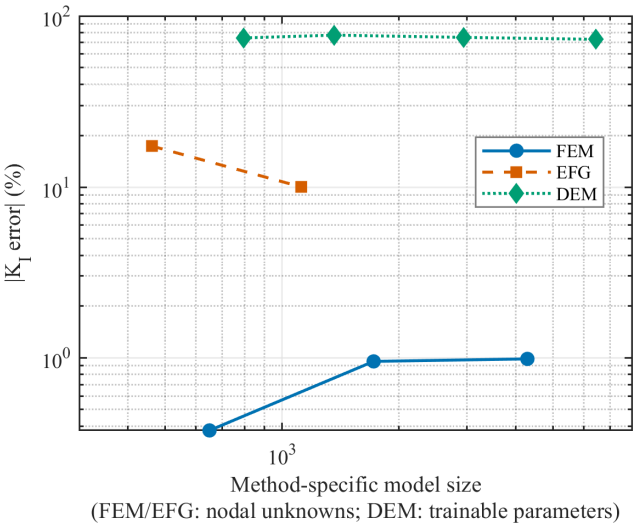


Fig. 10. Native-extraction crack K_I deviation relative to the nominal infinite-plate value. FEM and EFG use spatial refinement; DEM uses network-width variation. At the finest tested configurations, the absolute deviations are 0.38% (FEM), 10.04% (EFG), and 73.06% (DEM). The separate shared-grid check converges at 160×160 to 0.33%, 9.02%, and 73.13%. Nodal unknowns and trainable parameters are method-specific coordinates and are not resolution-equivalent.

Table 4. Descriptive audit of DEM loss-based trial selection. A positive ρ means that lower final loss tends to accompany lower error. The finite-trial range pools all sampled widths and summarizes observed variability; no formal significance claim is made, and no confidence interval or hypothesis test is reported.

Problem	Accuracy metric	N	Agree	ρ	Interpretation; finite-trial error range
Cantilever, $\nu = 0.3$	Tip displacement	8	4/4	+0.98	informative; $0.39 - 36.77\%$
Cook's membrane, both ν values	Tip displacement	28	7/8	+0.69	informative; $0.03 - 5.08\%$
Plate with hole	Energy error	8	4/4	+1.00	informative; 5.577×10^{-3}–1.841×10^{-2}
Plate with hole	Hole-boundary σ_x error	8	3/4	+0.29	weak; $56.78 - 115.65\%$
Crack	K_I error	8	2/4	0.00	uninformative; $73.06 - 77.32\%$
Cantilever, $\nu = 0.4999$	Tip displacement	14 finite	0/4	-0.92	inverse ordering; $73.49 - 96.48\%$

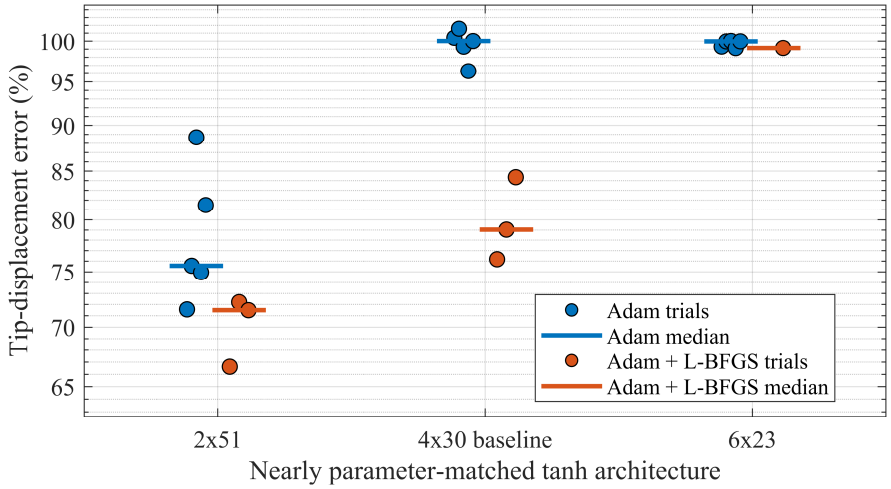


Fig. 11. Nearly parameter-matched DEM sensitivity study for the $\nu = 0.4999$ cantilever. Points and horizontal bars show finite trial errors and their medians after Adam and after Adam plus L-BFGS. The non-finite L-BFGS outcomes, 2/5 for 2×51, 2/5 for 4×30, and 4/5 for 6×23, are not plotted.

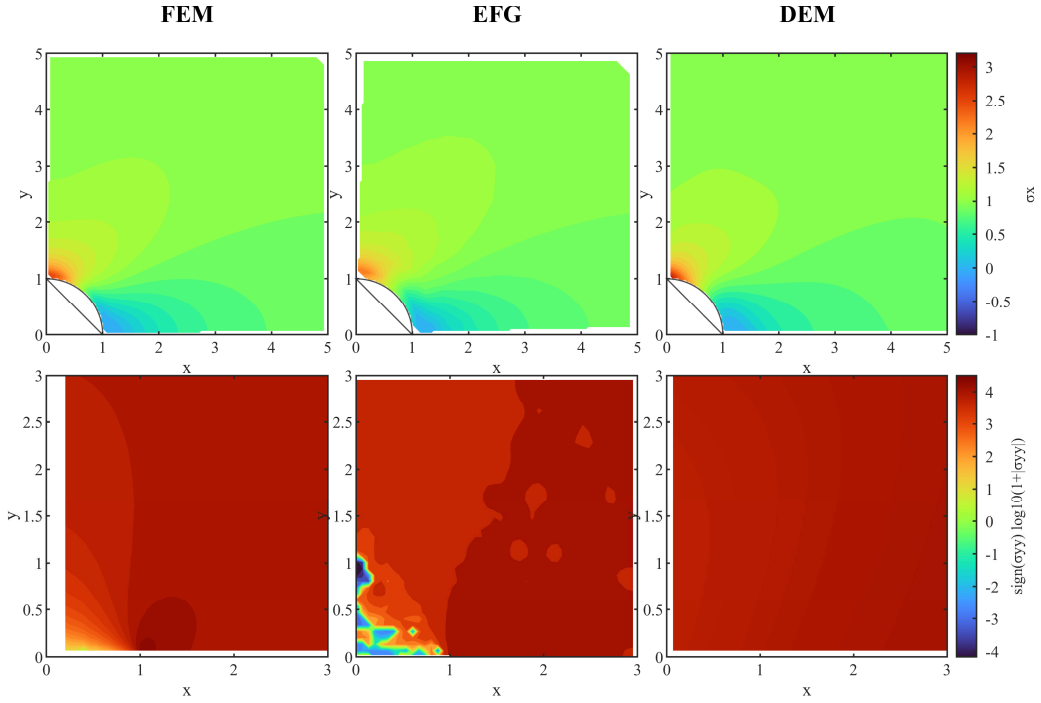


Fig. 12. Stress-field contours for the crack and plate-with-hole problems, from the field data exported for each method. The DEM crack field is visibly flatter near the tip than the FEM and EFG fields, and the hole fields share the global Kirsch pattern while differing in peak resolution.

The matched-parameter sensitivity study quantifies configuration dependence. The 2×51, 4×30, and 6×23 tanh networks contain 2909, 2942, and 2877 parameters. All fifteen Adam stages remain finite, with median tip errors of 75.57%, 100.02%, and 99.97%. Subsequent L-BFGS refinement becomes non-finite in 2/5, 2/5, and 4/5 runs. Among the finite outcomes, median errors are 71.49%, 79.03%, and 99.15%. L-BFGS reduces the median finite error for the two- and four-layer networks while also producing non-finite outcomes; the six-layer network remains inaccurate. Both network depth and optimizer stage therefore affect the tested DEM configuration.

Table 5. Accuracy-matched wall-clock comparison. Each entry is the time of the first tested configuration meeting the stated target; timings are single measurements on the hardware in Section 3.2.

Problem and common target	FEM (s)	EFG (s)	DEM (s)
Cantilever, $\nu = 0.3$: tip error $< 1\%$	0.190	0.150	1136
Cook, $\nu = 0.3$: Q8-reference tip error $< 1\%$	0.080	2.277	2459
Cantilever, $\nu = 0.4999$: tip error $< 1\%$	Not reached	8.445	Not reached
Plate with hole: energy error $< 6 \times 10^{-3}$	0.016	0.663	738
Crack: $\lvert K_I \rvert$ deviation $< 20\%$ of nominal	0.037	2.420	Not reached

5.8. Stress fields and computational cost

Figure 12 compares the available stress-field exports. The plots support the numerical trends qualitatively: the DEM crack field is visibly flatter near the tip, and the hole fields share the global Kirsch pattern while differing in peak resolution. Because the exported fields use different sampling grids and extents, the contours are illustrative rather than a common-grid error test.

Figure 13 shows error versus wall-clock time on the stated hardware. Because model-size coordinates are not commensurate, this is the primary cross-method efficiency comparison. Table 5 additionally reports the first tested configuration that reaches the same problem-specific accuracy target. The timings are single measurements of these implementations, not hardware-independent complexity results.

Table 5 reports the first tested configuration that reaches each accuracy target. FEM and EFG require fractions of a second to seconds. DEM requires hundreds to thousands of seconds for the targets it reaches and does not attain the 1% near-incompressible cantilever or 20% crack target.

Figure 14 provides a compact descriptive summary of the tested formulations using the independent Q8 Cook reference, the shared near-hole ring, and the converged 160×160 crack grid. Its entries refer only to the specified baseline implementations and metrics; they do not define a decision rule for other FEM, EFG, or DEM variants.

5.9. Observed error-reduction slopes

Table 6 reports the spatial-refinement slopes for FEM and EFG. Table 7 separately reports DEM capacity-scaling slopes. This separation avoids treating network parameters as spatial degrees of freedom.

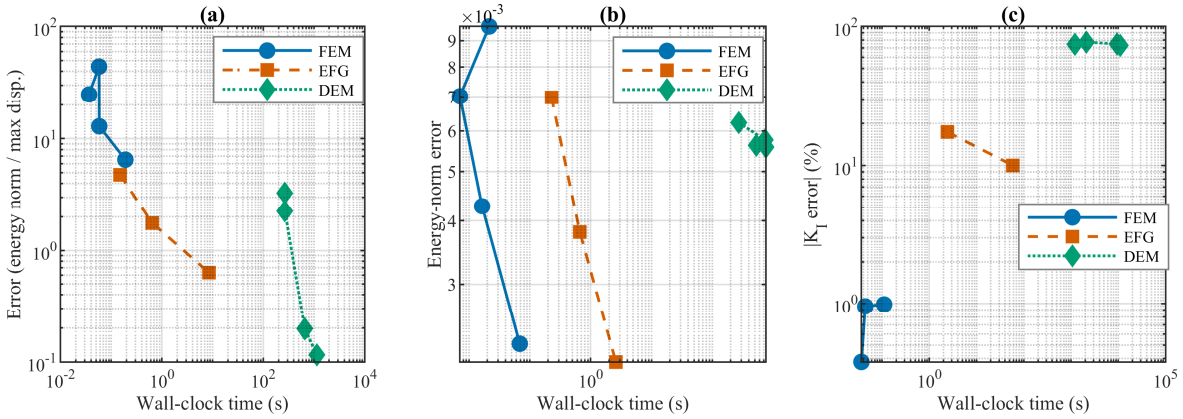


Fig. 13. Wall-clock time versus error for the implementations tested here (hardware and software detailed in Section 3.2). Repeated-timing statistics were not collected, so the comparison is not a hardware-independent complexity result.

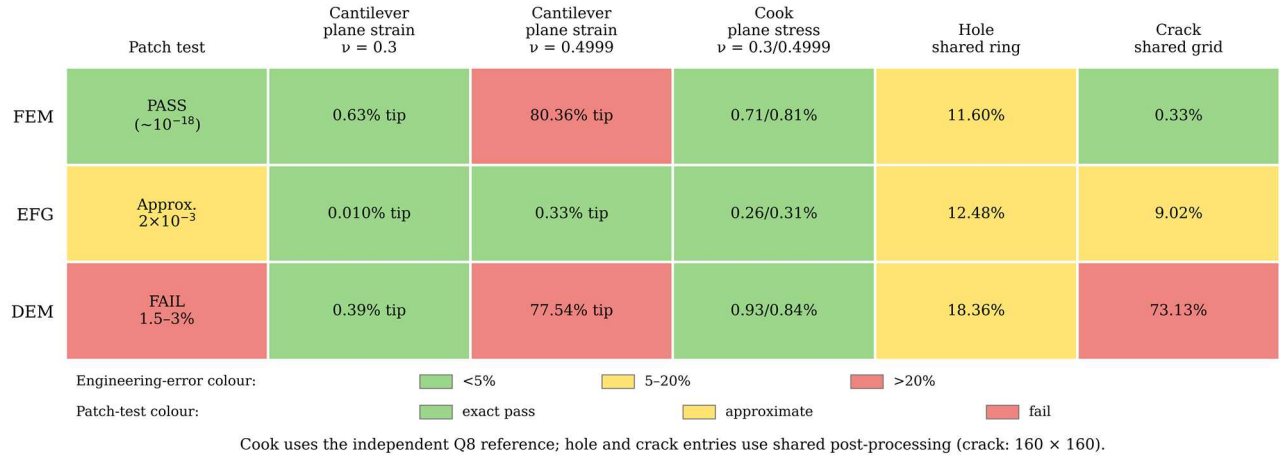


Fig. 14. Descriptive scorecard for the three tested baseline formulations and the selected common metric in each benchmark. For engineering-error cells, green denotes $< 5\%$, amber 5–20%, and red $> 20\%$. The patch-test column is classified separately as exact pass, approximate reproduction, or fail. Cook uses the independent Q8 reference; the hole entry uses $r = 1.01a$; and the crack entry uses the 160×160 shared interaction-integral grid. Enriched, mixed, stabilized, and adaptive variants are outside its scope.

Table 6. Observed spatial-refinement slopes for FEM and EFG. The EFG crack slope uses only two levels and is exact by construction; the FEM crack sequence is non-monotonic and near an already small error.

Problem/metric	FEM Rate	FEM R^2	FEM Mono.	EFG Rate	EFG R^2	EFG Mono.
Cantilever, $\nu = 0.3$, energy	0.51	1.00	Y	0.82	1.00	Y
Cantilever, $\nu = 0.4999$, energy	0.30	0.97	Y	0.95	0.99	Y
Plate with hole, energy	0.37	0.98	Y	0.66	1.00	Y
Plate with hole, boundary stress	0.38	0.99	Y	0.42	0.98	Y
Crack, K_I error	0.51	0.79	N	0.62	1.00	Y

Table 7. DEM error-reduction slopes against trainable parameter count. These are four-point capacity trends that mix representation and optimization; they are not classical convergence orders.

Problem/metric	Rate	R^2	Mono.
Cantilever, $\nu = 0.3$, maximum displacement error	1.78	0.92	Y
Cantilever, $\nu = 0.4999$, maximum displacement error	–0.10	0.96	N
Cantilever, $\nu = 0.3$, energy error	0.51	0.95	Y
Cantilever, $\nu = 0.4999$, energy error	0.24	0.99	Y
Plate with hole, energy error	0.05	0.76	Y
Plate with hole, boundary stress error	0.10	0.16	N
Crack, K_I error	0.01	0.30	N

For the smooth compressible cantilever, the FEM energy slope of 0.51 is consistent with the expected first-order value of 0.5. The EFG value of 0.82 over three levels is a pre-asymptotic observed slope, not evidence of superconvergence. The lower FEM hole slope cannot be attributed to singular regularity because the circular boundary is smooth; additional geometry and post-processing studies are required. The crack slopes are not reliable asymptotic estimates because the FEM sequence is non-monotonic and the EFG sequence has only two points. The corrected DEM cantilever energy-error slopes are 0.51 at $\nu = 0.3$ and 0.24 at $\nu = 0.4999$, both monotonic, whereas the corresponding maximum-displacement trends are 1.78 and –0.10. This difference reinforces that tip displacement and full-field energy error characterize distinct aspects of the trained field.

6. Discussion

The benchmark provides comparative evidence on interactions that isolated single-method studies do not resolve. Full-integration Q4 locking, MLS non-interpolation and penalty sensitivity, and optimization dependence in neural energy solvers are established. Under the common protocol, their effects vary with problem regime and quantity of interest. The selected localized ordering persists under shared-point post-processing, DEM loss-error association ranges from positive to inverse, and nearly fixed neural capacity does not eliminate sensitivity to depth and optimizer stage.

For the near-incompressible cantilever, the tested full-integration Q4 formulation locks strongly, while the tested first-order MLS EFG formulation reaches a tip displacement within 0.33% of the reference after refinement. EFG can alleviate or exhibit locking depending on support, integration, and stabilization choices [22, 23]. The result therefore shows that this EFG configuration is less locking-prone than this Q4 configuration for the present benchmark.

DEM's cantilever behavior differs from Q4 discretization locking. The baseline non-finite runs and inverse loss-error ordering identify optimization instability for the original four-layer schedule. In the matched-parameter study, eight of fifteen L-BFGS refinements become non-finite, and the finite median errors range from 71.49% to 99.15%. Cook's membrane remains accurate relative to the independent Q8 reference, but its plane-stress formulation does not provide an independent test of the plane-strain volumetric conditioning present in the cantilever. The present experiments therefore cannot disentangle plane-strain near-incompressibility, bending-dominated kinematics, boundary-condition construction, representation error, and optimizer conditioning.

The hole and crack results show why bulk energy accuracy is insufficient for localized engineering quantities. The energy objective integrates over the domain, whereas boundary stress and K_I depend on a small region and on the post-processing operator. On the common near-hole ring, FEM and EFG are close (11.60% and 12.48%) and both are below DEM (18.36%); the much larger native EFG boundary maximum is therefore strongly sampling-dependent. Exact Kirsch tractions are imposed on both finite outer edges for all three formulations, so the shared-ring discrepancy cannot be attributed to replacing the Kirsch boundary data by a uniform remote stress. For FEM and EFG it includes the chordal representation of the hole and numerical stress evaluation near that boundary. For the crack, the shared-grid sequence shows that the coarse-grid FEM sign change disappears with post-processing refinement, while the converged ordering remains FEM, EFG, then DEM. These findings apply to the conforming graded Q4 mesh, penalty EFG without crack-tip enrichment, and the unenriched tanh DEM.

The trial-selection audit shows that final loss identifies the best quantity of interest only when that quantity is strongly coupled to the loss and training remains stable. For the sampled near-incompressible cantilever trials, the minimum-loss choice selects the largest tip-displacement error at every width. Learning-based solver comparisons should therefore report all seeded outcomes, non-finite-run frequencies, and errors in the target engineering quantity.

The DEM implementation requires substantially more wall-clock time than the FEM and EFG direct-solve implementations for these small linear problems. The comparison is implementation-specific because it uses one hardware configuration and single timing measurements. Inverse, parametric, nonlinear, and high-dimensional settings may produce different cost relationships, but they are outside the present tests. The timing results therefore characterize the selected solvers for small forward elastostatic problems and do not establish hardware-independent computational complexity.

7. Limitations

The conclusions are bounded by the following four limitations:

- Scope of the tested formulations and problems. The comparison concerns full-integration Q4 FEM, first-order MLS EFG with a global essential-boundary penalty, and specified tanh DEM configurations on five small-strain, isotropic, static, two-dimensional problems. The matched-capacity DEM study broadens the neural evidence across depth and optimizer stage but does not convert implementation-level findings into family-wide conclusions. Mixed, reduced-integration, enriched, stabilized, adaptive, and higher-order benchmark variants remain outside the comparison.
- Evaluation grids and refinement variables. Bulk error integrals use method-specific quadrature and sampling. The shared near-hole ring and the 40×40, 80×80, and 160×160 crack sequence improve the localized comparison but do not re-evaluate every full-domain error on one grid. The hole ring is offset from the exact boundary to remain inside the chordal Q4 geometry. FEM/EFG nodal unknowns and DEM trainable parameters remain non-equivalent capacity coordinates.
- Stochastic sample and mechanistic ablations. Most baseline DEM configurations have two seeds, with five for the two $\nu = 0.4999$ problems. The depth study uses five seeds for three nearly parameter-matched architectures and evaluates both Adam and L-BFGS stages, but it is confined to the near-incompressible cantilever. Activation, collocation density, boundary ansatz, learning rate, and mixed pressure output are not varied, so the study does not fully separate representation error from optimization error.
- Reference values. Cook's membrane is compared with an independent Q8 convergence sequence; its final values change by less than 0.05% from the preceding level but remain numerical references. For the hole problem, the Kirsch stress tensor supplies both the analytical reference and, after multiplication by the outward normal, the traction imposed on the finite outer edges. The finite outer extent therefore does not introduce a boundary-data mismatch, although the FEM and EFG chordal hole geometry and their numerical stress evaluation prevent the Kirsch field from being an exact discrete-domain solution. The crack is normalized by the infinite-plate Irwin value although its modeled domain is finite. The crack results are thus deviations from a common analytical normalization, supplemented by shared post-processing, rather than certified errors for the finite computational domain.

8. Conclusion

This paper compared specified FEM, EFG, and DEM formulations on five two-dimensional linear-elastostatic problems. Its contribution is a controlled cross-paradigm assessment of how formulation-specific behavior changes with physical regime, quantity of interest, and measured computational effort.

First, no tested formulation is uniformly best. Full-integration Q4 FEM is strongly over-stiff in the near-incompressible plane-strain cantilever, while the tested EFG formulation reaches 0.33% tip error. All three formulations reach below 1% on plane-stress Cook's membrane relative to an independent Q8 reference, but this different stress state does not isolate the cause of the cantilever behavior. On the shared near-hole ring FEM and EFG are close, and the converged shared crack check preserves the FEM-EFG-DEM ordering for the specified implementations.

Second, DEM performance depends on the quantity, problem, architecture, and optimizer stage. The tested configurations reproduce Cook's membrane closely but remain inaccurate for the near-incompressible cantilever. In the matched-parameter study, eight of fifteen L-BFGS refinements become non-finite, and finite median errors range from 71.49% to 99.15%. These results quantify sensitivity within the tested design space and do not define a performance limit for energy-based learning.

Third, final training loss is not a universal model-selection criterion. It orders some sampled bulk quantities but has weak association with localized stress and K_I and inverse ordering with the near-incompressible cantilever tip error. A minimum-loss result alone does not report non-finite runs or the observed variation in engineering error. Seeded outcomes, non-finite-run frequencies, and the target quantity should be reported.

Finally, cross-method comparison should use physical error and measured effort rather than equating trainable parameters with nodal unknowns. The accuracy-threshold comparison shows large implementation-level cost differences, while the absence of repeated timing and memory measurements limits complexity claims. Future benchmark suites should include mixed and enriched formulations, broader neural ablations, independent finite-domain fracture references, memory accounting, and three-dimensional or nonlinear problems. Dynamic extensions should assess accuracy, stability, temporal resolution, and cost under transient loading, including the large-time-step PINN setting examined by Qi et al. [88].

Author Contributions

T. Yang planned the study, initiated the project, designed the experiments, and conducted the computations. A. Qarariyah developed the mathematical formulation, analyzed the numerical results, and examined the study limitations. Both authors contributed to writing, reviewing, and approving the final manuscript.

Acknowledgments

The authors gratefully acknowledge the support of their colleagues at the Engineering Model and Design (E-MoDe) Research Group (RG-BU008), Deanship of Graduate Studies and Scientific Research, Bethlehem University.

Conflict of Interest

The authors declared no potential conflicts of interest concerning the research, authorship, and publication of this article.

Funding

T. Yang is supported by the National Natural Science Foundation of China (No. 12401502). A. Qarariyah is supported by Internal Research Grant #IRG/2025/002, Deanship of Graduate Studies and Scientific Research, Bethlehem University.

Data Availability Statement

The solver source and complete configuration files are available from the corresponding author upon reasonable request.

References

[1] Belytschko, T., Lu, Y.Y., Gu, L., Element-free Galerkin methods, *International Journal for Numerical Methods in Engineering*, 37, 1994, 229-256.
[2] Nguyen-Thanh, V.M., Zhuang, X., Rabczuk, T., A deep energy method for finite deformation hyperelasticity, *European Journal of Mechanics-A/Solids*, 80, 2020, 103874.
[3] Nguyen, V.P., Rabczuk, T., Bordas, S. et al., Meshless methods: a review and computer implementation aspects, *Mathematics and Computers in Simulation*, 79, 2008, 763-813.
[4] Liu, G.R., *Meshfree methods: moving beyond the finite element method*, CRC Press, 2002.
[5] Belytschko, T., Krongauz, Y., Organ, D. et al., Meshless methods: an overview and recent developments, *Computer Methods in Applied Mechanics and Engineering*, 139, 1996, 3-47.
[6] Li, X., Li, S., An efficient and consistent gradient polynomial smoothing integration algorithm for Galerkin meshfree methods with explicit quadrature, *Journal of Computational Physics*, 563, 2026, 115122.
[7] Thawon, I., Vo, D., Bui, T.Q. et al., Physics-informed neural networks: current progress and challenges in computational solid and structural mechanics, *CMES-Computer Modeling in Engineering and Sciences*, 146, 2026, 2.
[8] Thombre, M., Anitescu, C., Bharadwaja, B.V.S.S. et al., Energy-based methods for solving forward and inverse linear elasticity problems in 2D structures, *Computers & Structures*, 316, 2025, 107899.
[9] Grossmann, T.G., Komorowska, U.J., Latz, J., Schönlieb, C.-B., Can physics-informed neural networks beat the finite element method?, *IMA Journal of Applied Mathematics*, 89(1), 2024, 143-174.
[10] Abueidda, D.W., Lu, Q., Koric, S., Meshless physics-informed deep learning method for three-dimensional solid mechanics, *International Journal for Numerical Methods in Engineering*, 122, 2021, 7182-7201.
[11] Bai, J., Rabczuk, T., Gupta, A. et al., A physics-informed neural network technique based on a modified loss function for computational 2D and 3D solid mechanics, *Computational Mechanics*, 71, 2023, 543-562.
[12] Moës, N., Dolbow, J., Belytschko, T., A finite element method for crack growth without remeshing, *International Journal for Numerical Methods in Engineering*, 46, 1999, 131-150.
[13] Belytschko, T., Black, T., Elastic Crack Growth in Finite Elements with Minimal Remeshing, *International Journal for Numerical Methods in Engineering*, 45, 1999, 601-620.
[14] Sukumar, N., Chopp, D.L., Moës, N. et al., Modeling Holes and Inclusions by Level Sets in the Extended Finite-Element Method, *Computer Methods in Applied Mechanics and Engineering*, 190, 2001, 6183-6200.
[15] Babuška, I., Melenk, J.M., The partition of unity method, *International Journal for Numerical Methods in Engineering*, 40, 1997, 727-758.
[16] Francfort, G.A., Marigo, J.J., Revisiting Brittle Fracture as an Energy Minimization Problem, *Journal of the Mechanics and Physics of Solids*, 46, 1998, 1319-1342.
[17] Bourdin, B., Francfort, G.A., Marigo, J.J., The variational approach to fracture, *Journal of Elasticity*, 91, 2008, 5.
[18] Miehe, C., Welschinger, F., Hofacker, M., Thermodynamically consistent phase-field models of fracture: Variational principles and multi-field FE implementations, *International Journal for Numerical Methods in Engineering*, 83, 2010, 1273-1311.
[19] Griffith, A.A., The Phenomena of Rupture and Flow in Solids, *Philosophical Transactions of the Royal Society of London Series A*, 221, 1921, 163-198.
[20] Cervera, M., Barbat, G., Chiumenti, M. et al., A comparative review of XFEM, mixed FEM and phase-field models for quasi-brittle cracking, *Archives of Computational Methods in Engineering*, 29, 2022, 1009-1083.
[21] Nayroles, B., Touzot, G., Villon, P., Generalizing the finite element method: diffuse approximation and diffuse elements, *Computational Mechanics*, 10, 1992, 307-318.
[22] Askes, H., de Borst, R., Heeres, O., Conditions for locking-free elasto-plastic analyses in the Element-Free Galerkin method, *Computer Methods in Applied Mechanics and Engineering*, 173, 1999, 99-109.
[23] Huerta, A., Fernández-Méndez, S., Locking in the incompressible limit for the element-free Galerkin method, *International Journal for Numerical Methods in Engineering*, 51, 2001, 1361-1383.
[24] Liu, W.K., Jun, S., Zhang, Y.F., Reproducing kernel particle methods, *International Journal for Numerical Methods in Fluids*, 20, 1995, 1081-1106.
[25] Atluri, S.N., Zhu, T., A new meshless local Petrov-Galerkin (MLPG) approach in computational mechanics, *Computational Mechanics*, 22, 1998, 117-127.
[26] Duarte, C., Oden, J., H-p clouds: an h-p meshless method, *Numerical Methods for Partial Differential Equations*, 12, 1996, 673-705.
[27] Liu, G.R., Gu, Y., A point interpolation method for two-dimensional solids, *International Journal for Numerical Methods in Engineering*, 50, 2001, 937-951.
[28] Sukumar, N., Moran, B., Belytschko, T., The natural element method in solid mechanics, *International Journal for Numerical Methods in Engineering*, 43, 1998, 839-887.
[29] Rvachev, V., Sheiko, T., R-functions in boundary value problems in mechanics, *Applied Mechanics Reviews*, 48, 1995, 151-188.
[30] Höllig, K., Reif, U., Wipper, J., Weighted extended B-spline approximation of Dirichlet problems, *SIAM Journal on Numerical Analysis*, 39, 2001, 442-462.
[31] Yang, T., Qarariyah, A., Deng, J., Spline R-function and applications in FEM, *Numerical Mathematics: Theory, Methods and Applications*, 13, 2020, 150-175.
[32] Qarariyah, A., Yang, T., Deng, F., A solution-structure B-spline-based framework for hybrid boundary problems on implicit domains, *Mathematics*, 12, 2024, 3973.
[33] Raissi, M., Perdikaris, P., Karniadakis, G.E., Physics-informed neural networks: A deep learning framework for solving forward and inverse problems involving nonlinear partial differential equations, *Journal of Computational physics*, 378, 2019, 686-707.
[34] Karniadakis, G.E., Kevrekidis, I.G., Lu, L. et al., Physics-Informed Machine Learning, *Nature Reviews Physics*, 3, 2021, 422-440.
[35] Weinan, E., Yu, B., The Deep Ritz Method: A Deep Learning-Based Numerical Algorithm for Solving Variational Problems, *Communications in Mathematics and Statistics*, 6, 2018, 1-12.
[36] Samaniego, E., Anitescu, C., Goswami, S. et al., An energy approach to the solution of partial differential equations in computational mechanics via machine learning: Concepts, implementation and applications, *Computer Methods in Applied Mechanics and Engineering*, 362, 2020, 112790.
[37] Lin, Z., Du, K., Li, Z., A Mesh-Free Physics-Informed Neural Network Framework for Solving Plane Problems without Locking Issues, *Journal of Applied and Computational Mechanics*, 12(3), 2026, 1047-1068.
[38] Jagtap, A.D., Karniadakis, G.E., Extended physics-informed neural networks (XPINNs): A generalized space-time domain decomposition based deep learning framework for nonlinear partial differential equations, *Communications in Computational Physics*, 28, 2020, 2002-2041.
[39] Jagtap, A.D., Kharazmi, E., Karniadakis, G.E., Conservative Physics-Informed Neural Networks on Discrete Domains for Conservation Laws: Applications to Forward and Inverse Problems, *Computer Methods in Applied Mechanics and Engineering*, 365, 2020, 113028.
[40] Moseley, B., Markham, A., Nissen-Meyer, T., Finite Basis Physics-Informed Neural Networks (FBPINNs): A Scalable Domain Decomposition Approach for Solving Differential Equations, *Advances in Computational Mathematics*, 49, 2023, 62.
[41] Kharazmi, E., Zhang, Z., Karniadakis, G.E., hp-VPINNs: Variational physics-informed neural networks with domain decomposition, *Computer Methods in Applied Mechanics and Engineering*, 374, 2021, 113547.
[42] Wang, S., Teng, Y., Perdikaris, P., Understanding and mitigating gradient flow pathologies in physics-informed neural networks, *SIAM Journal on Scientific Computing*, 43, 2021, A3055-A3081.
[43] Wang, S., Yu, X., Perdikaris, P., When and why PINNs fail to train: A neural tangent kernel perspective, *Journal of Computational Physics*, 449, 2022, 110768.
[44] Krishnapriyan, A., Gholami, A., Zhe, S. et al., Characterizing possible failure modes in physics-informed neural networks, *Advances in Neural Information Processing Systems*, 34, 2021, 26548-26560.
[45] McClenny, L.D., Braga-Neto, U.M., Self-Adaptive Physics-Informed Neural Networks, *Journal of Computational Physics*, 474, 2023, 111722.
[46] Anagnostopoulos, S.J., Toscano, J.D., Stergiopulos, N. et al., Residual-Based Attention in Physics-Informed Neural Networks, *Computer Methods in Applied Mechanics and Engineering*, 421, 2024, 116805.
[47] Lu, L., Meng, X., Mao, Z. et al., DeepXDE: A deep learning library for solving differential equations, *SIAM Review*, 63, 2021, 208-228.
[48] Abueidda, D.W., Koric, S., Al-Rub, R.A. et al., A deep learning energy method for hyperelasticity and viscoelasticity, *European Journal of Mechanics-*

A/Solids, 95, 2022, 104639.
[49] Fuhg, J.N., Bouklas, N., The mixed deep energy method for resolving concentration features in finite strain hyperelasticity, *Journal of Computational Physics*, 451, 2022, 110839.
[50] Chadha, C., He, J., Abueidda, D. et al., Improving the accuracy of the deep energy method, *Acta Mechanica*, 234, 2023, 5975-5998.
[51] He, J., Abueidda, D., Koric, S. et al., On the use of graph neural networks and shape-function-based gradient computation in the deep energy method, *International Journal for Numerical Methods in Engineering*, 124, 2023, 864-879.
[52] He, J., Chadha, C., Kushwaha, S. et al., Deep energy method in topology optimization applications, *Acta Mechanica*, 234, 2023, 1365-1379.
[53] Gu, Y., Zhang, C., Zhang, P. et al., Enriched physics-informed neural networks for 2D in-plane crack analysis: Theory and MATLAB code, *International Journal of Solids and Structures*, 276, 2023, 112321.
[54] Baek, J., Chen, J.S., Susuki, K., A neural network-enhanced reproducing kernel particle method for modeling strain localization, *International Journal for Numerical Methods in Engineering*, 123, 2022, 4422-4454.
[55] Baek, J., Chen, J.S., A neural network-based enrichment of reproducing kernel approximation for modeling brittle fracture, *Computer Methods in Applied Mechanics and Engineering*, 419, 2024, 116590.
[56] Qarariyah, A., Yang, T., Deng, F., An intelligent SPH framework based on machine-learned residual correction for elliptic PDEs, *Algorithms*, 18, 2025, 803.
[57] Du, H., He, Q., Neural-Integrated Meshfree (NIM) Method: A differentiable programming-based hybrid solver for computational mechanics, *Computer Methods in Applied Mechanics and Engineering*, 427, 2024, 117024.
[58] Du, H., Guo, B., He, Q., Differentiable Neural-Integrated Meshfree Method for Forward and Inverse Modeling of Finite Strain Hyperelasticity, *Engineering with Computers*, 41, 2025, 1597–1617.
[59] Wang, Y., Sun, J., Li, W. et al., CENN: Conservative energy method based on neural networks with subdomains for solving variational problems involving heterogeneous and complex geometries, *Computer Methods in Applied Mechanics and Engineering*, 400, 2022, 115491.
[60] Timoshenko, S.P., Goodier, J.N., *Theory of Elasticity*, McGraw-Hill, 1970.
[61] Kirsch, G., Die Theorie der Elastizität und die Bedürfnisse der Festigkeitslehre, *Zeitschrift des Vereines Deutscher Ingenieure*, 42, 1898, 797-807.
[62] Irwin, G.R., Analysis of Stresses and Strains Near the End of a Crack Traversing a Plate, *Journal of Applied Mechanics*, 24, 1957, 361-364.
[63] Williams, M.L., On the Stress Distribution at the Base of a Stationary Crack, *Journal of Applied Mechanics*, 24, 1957, 109-114.
[64] Hughes, T.J.R., *The Finite Element Method: Linear Static and Dynamic Finite Element Analysis*, Courier Corporation, 2003.
[65] Belytschko, T., Liu, W.K., Moran, B. et al., *Nonlinear Finite Elements for Continua and Structures*, John Wiley & Sons, 2014.
[66] Belytschko, T., Lu, Y.Y., Gu, L. et al., Element-Free Galerkin Methods for Static and Dynamic Fracture, *International Journal of Solids and Structures*, 32, 1995, 2547-2570.
[67] Lancaster, P., Salkauskas, K., Surfaces Generated by Moving Least Squares Methods, *Mathematics of Computation*, 37, 1981, 141-158.
[68] Armentano, M.G., Durán, R.G., Error Estimates for Moving Least Square Approximations, *Applied Numerical Mathematics*, 37, 2001, 397-416.
[69] Wendland, H., Local Polynomial Reproduction and Moving Least Squares Approximation, *IMA Journal of Numerical Analysis*, 21, 2001, 285-300.
[70] Babuška, I., The Finite Element Method with Lagrangian Multipliers, *Numerische Mathematik*, 20, 1973, 179-192.
[71] Lu, Y.Y., Belytschko, T., Gu, L., A New Implementation of the Element Free Galerkin Method, *Computer Methods in Applied Mechanics and Engineering*, 113, 1994, 397-414.
[72] Chen, J.S., Wang, H.P., New Boundary Condition Treatments in Meshfree Computation of Contact Problems, *Computer Methods in Applied Mechanics and Engineering*, 187, 2000, 441-468.
[73] Cybenko, G., Approximation by Superpositions of a Sigmoidal Function, *Mathematics of Control, Signals and Systems*, 2, 1989, 303-314.
[74] Hornik, K., Stinchcombe, M., White, H., Multilayer Feedforward Networks Are Universal Approximators, *Neural Networks*, 2, 1989, 359-366.
[75] Hornik, K., Approximation Capabilities of Multilayer Feedforward Networks, *Neural Networks*, 4, 1991, 251-257.
[76] Leshno, M., Lin, V.Y., Pinkus, A. et al., Multilayer Feedforward Networks with a Nonpolynomial Activation Function Can Approximate Any Function, *Neural Networks*, 6, 1993, 861-867.
[77] Mishra, S., Molinaro, R., Estimates on the Generalization Error of Physics-Informed Neural Networks for Approximating PDEs, *IMA Journal of Numerical Analysis*, 43, 2023, 1-43.
[78] Lagaris, I.E., Likas, A., Fotiadis, D.I., Artificial Neural Networks for Solving Ordinary and Partial Differential Equations, *IEEE Transactions on Neural Networks*, 9, 1998, 987-1000.
[79] Baydin, A.G., Pearlmutter, B.A., Radul, A.A. et al., Automatic Differentiation in Machine Learning: A Survey, *Journal of Machine Learning Research*, 18, 2018, 1-43.
[80] Kingma, D.P., Ba, J., Adam: A Method for Stochastic Optimization, *3rd International Conference on Learning Representations (ICLR)*, 2015.
[81] Reddi, S.J., Kale, S., Kumar, S., On the Convergence of Adam and Beyond, *International Conference on Learning Representations (ICLR)*, 2018.
[82] Liu, D.C., Nocedal, J., On the limited memory BFGS method for large scale optimization, *Mathematical Programming*, 45, 1989, 503-528.
[83] Nocedal, J., Wright, S.J., *Numerical Optimization*, Springer, 2006.
[84] Zhu, C., Byrd, R.H., Lu, P. et al., Algorithm 778: L-BFGS-B, FORTRAN Subroutines for Large Scale Bound Constrained Optimization, *ACM Transactions on Mathematical Software*, 23, 1997, 550-560.
[85] Irons, B.M., Razzaque, A., Experience with the Patch Test for Convergence of Finite Elements, *The Mathematical Foundations of the Finite Element Method with Applications to Partial Differential Equations*, 1972, 557-587.
[86] Cook, R.D., Improved two-dimensional finite element, *Journal of the Structural Division*, 100, 1974, 1851-1863.
[87] Fleming, M., Chu, Y.A., Moran, B. et al., Enriched Element-Free Galerkin Methods for Crack Tip Fields, *International Journal for Numerical Methods in Engineering*, 40, 1997, 1483-1504.
[88] Qi, J., Du, K., Luo, H., Wang, Z., Wen, R., Physics-Informed Neural Networks for Structural Dynamic Response Analysis: Theoretical and Numerical Verification, *International Journal of Structural Stability and Dynamics*, 27, 2027, 2650294.

ORCID iD

Tianhui Yang https://orcid.org/0000-0003-1732-6405
Ammar Qarariyah https://orcid.org/0000-0003-3869-1268

© 2026 Shahid Chamran University of Ahvaz, Ahvaz, Iran. This article is an open access article distributed under the terms and conditions of the Creative Commons Attribution-NonCommercial 4.0 International (CC BY-NC 4.0 license) (http://creativecommons.org/licenses/by-nc/4.0/).

How to cite this article: Yang T., Qarariyah A. From Elements to Energy: A Controlled Benchmark of Finite Element, Element-Free Galerkin, and Deep Energy Methods in Solid Mechanics, *J. Appl. Comput. Mech.*, xx(x), 2026, 1–18. https://doi.org/10.22055/jacm.2026.49665.6145

Publisher's Note Shahid Chamran University of Ahvaz remains neutral with regard to jurisdictional claims in published maps and institutional affiliations.